

Gravitational-wave physics with Cosmic Explorer: Limits to low-frequency sensitivity

Evan D. Hall¹, Kevin Kuns¹, Joshua R. Smith², Yuntao Bai,³ Christopher Wipf,⁴ Sebastien Biscans^{4,1},
Rana X Adhikari,⁴ Koji Arai⁴, Stefan Ballmer⁵, Lisa Barsotti¹, Yanbei Chen,³ Matthew Evans,¹
Peter Fritschel,¹ Jan Harms,^{6,7} Brittany Kamai^{8,9}, Jameson Graef Rollins⁴, David Shoemaker¹,
Bram J. J. Slagmolen¹⁰, Rainer Weiss,¹ and Hiro Yamamoto⁴

¹*LIGO Laboratory, Massachusetts Institute of Technology, Cambridge, Massachusetts 02139, USA*

²*Nicholas and Lee Begovich Center for Gravitational-Wave Physics and Astronomy,
California State University, Fullerton, Fullerton, California 92831, USA*

³*Walter Burke Institute for Theoretical Physics, California Institute of Technology,
Pasadena, California 91125, USA*

⁴*LIGO Laboratory, California Institute of Technology, Pasadena, California 91125, USA*

⁵*Department of Physics, Syracuse University, Syracuse, New York 13244, USA*

⁶*Gran Sasso Science Institute (GSSI), I-67100 L'Aquila, Italy*

⁷*INFN, Laboratori Nazionali del Gran Sasso, I-67100 Assergi, Italy*

⁸*Department of Astronomy and Astrophysics, University of California Santa Cruz,
Santa Cruz, California 95064, USA*

⁹*Department of Mechanical and Civil Engineering, California Institute of Technology,
Pasadena, California 91125, USA*

¹⁰*OzGrav, ANU Centre for Gravitational Astrophysics, Research Schools of Physics, and Astronomy and
Astrophysics, The Australian National University, Canberra, Australian Capital Territory 2601, Australia*



(Received 24 January 2021; accepted 13 May 2021; published 21 June 2021)

Cosmic Explorer is a next-generation ground-based gravitational-wave observatory concept, envisioned to begin operation in the 2030s and expected to be capable of observing binary neutron star and black hole mergers back to the time of the first stars. Cosmic Explorer's sensitive band will extend below 10 Hz, where the design is predominantly limited by geophysical, thermal, and quantum noises. In this work, thermal, seismic, gravity-gradient, quantum, residual gas, scattered-light, and servo-control noises are analyzed in order to motivate facility and vacuum system design requirements, potential test mass suspensions, Newtonian noise reduction strategies, improved inertial sensors, and cryogenic control requirements. Our analysis shows that, with improved technologies, Cosmic Explorer can deliver a strain sensitivity better than $10^{-23} \text{ Hz}^{-1/2}$ down to 5 Hz. Our work refines and extends previous analysis of the Cosmic Explorer concept and outlines the key research areas needed to make this observatory a reality.

DOI: [10.1103/PhysRevD.103.122004](https://doi.org/10.1103/PhysRevD.103.122004)

I. INTRODUCTION

The second generation of laser interferometric gravitational-wave observatories—the Advanced Laser Interferometer Gravitational-Wave Observatory (LIGO) [1], Advanced Virgo [2], and Kagra [3]—have opened a new window on the Universe by observing gravitational waves from merging systems of black holes [4,5] and neutron stars [6] and have ushered in a new era in multimessenger astronomy [7]. Dozens of coalescing binary systems have been observed thus far [8,9], with rapid alerts delivering sky locations and probable system types [10], bringing the features of the underlying astrophysical populations into focus. An enhancement to Advanced LIGO, known as LIGO A+, with improved quantum noise and optical coatings, is now being implemented [11]. Additionally, research and development is

underway toward a cryogenic silicon detector, LIGO Voyager, that could be implemented in the existing LIGO facilities [12], and a concept for a high-frequency-focused Australian observatory is being developed [13].

A vision is developing for a global third-generation (3G) network of ground-based gravitational-wave observatories capable of observing gravitational waves across cosmic time, with nearby systems detected with incredible precision [14,15]. The European concept for a third-generation observatory is the Einstein Telescope (ET) [16], a 10 km triangular underground observatory combining three high-power room-temperature interferometers sensitive at high frequency and three cryogenic silicon interferometers sensitive at low frequency. A U.S. concept for a 3G observatory is Cosmic Explorer [17–19], a 40 km L-shaped, single-interferometer observatory built on the Earth's surface.

We anticipate a staged approach to Cosmic Explorer, similar to the approach adopted by LIGO, in which the facility hosts successive generations of detectors, each exploiting the most advanced technology available at the time. We envision that the first detector, Cosmic Explorer 1 (CE1), will operate in the 2030s using LIGO A+ technology scaled up to the increased dimensions of the facility and with a few modest improvements. For the 2040s, the state-of-the-art technology is more difficult to predict. In this work we consider two possible designs for this detector, called Cosmic Explorer 2 (CE2). One possibility is that CE2 is a further extension of LIGO A+ technology, retaining room-temperature fused silica test masses and a $1\ \mu\text{m}$ laser as the working technology. Another possibility is that CE2 is an extension of the LIGO Voyager technology, employing silicon test masses at 123 K and a $2\ \mu\text{m}$ laser. In the rest of the paper, we will refer to detectors based on room-temperature fused silica test masses and $1\ \mu\text{m}$ laser wavelength as the “ $1\ \mu\text{m}$ technology” and those with cryogenic silicon test masses and $2\ \mu\text{m}$ laser wavelength as the “ $2\ \mu\text{m}$ technology.” For both CE1 and CE2, the detector designs target observations above 5 Hz, while Einstein Telescope targets observations down to 3 Hz.

This paper presents an assessment of the low-frequency sensitivity of CE1 and CE2 based on recent research and development progress. We first present the basic low-frequency observational capabilities of Cosmic Explorer (Sec. II) and discuss broadly the limits to the Cosmic Explorer strain sensitivities (Sec. III). We then describe the Cosmic Explorer facility (Sec. IV) and go into detail about low-frequency noise sources (Sec. V). Then in Sec. VI we take stock of the research and development that will be required to realize Cosmic Explorer and we look forward to future work. Appendix A summarizes the different technologies used in the two stages of Cosmic Explorer and Appendix B compares the displacement and force noises of Cosmic Explorer with those of other detectors.

II. ASTROPHYSICS

Cosmic Explorer has a range of science goals, which together take advantage of the instrument’s full broadband sensitivity up to several kilohertz. Here we focus on the detection of compact binary signals. The low-frequency sensitivity affects the reach of the instrument for heavy and high-redshift signals, as well as the total signal-to-noise ratio of all compact-binary signals. The optimal signal-to-noise ratio for a particular frequency-domain signal $h(f)$, measured in a detector with a strain noise power spectral density (PSD) S_h and a gravitational-wave sensitivity band extending down to a low-frequency cutoff f_{low} , is obtained when the signal is detected with a matched filter, yielding an amplitude signal-to-noise ratio ρ given by $\rho^2 = 4 \int_{f_{\text{low}}}^{\infty} df |h(f)|^2 / S_h(f)$ [20–22].

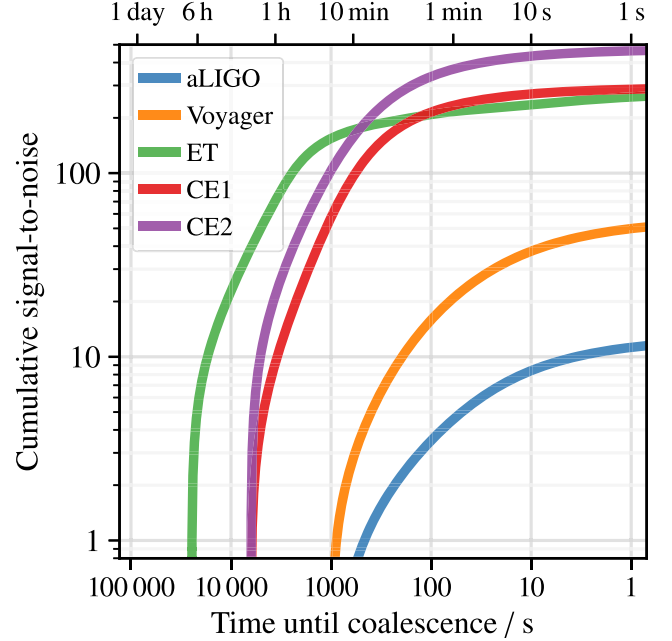


FIG. 1. Signal-to-noise ratio (SNR) accumulation of a $1.4 + 1.4 M_{\odot}$ binary neutron star system at redshift $z = 0.03$, optimally oriented. The low-frequency cutoffs are the same as given in Fig. 2. Numerical early warning values for a threshold signal-to-noise ratio of 8 are given in Table I, showing that third-generation detectors will provide early warning on the scale of hours, compared to the minutes provided by second-generation detectors. Systems this loud (or louder) should be expected roughly once per year assuming a local merger rate of $\sim 300\ \text{Gpc}^{-3}\ \text{yr}^{-1}$ [24].

For light systems (e.g., neutron stars) which are still in their inspiral phase at frequencies $f \lesssim 10$ Hz, improving the low-frequency cutoff f_{low} has a modest but noticeable improvement on the total signal-to-noise ratio: for the idealized case of a detector with a flat noise floor down to a lower cutoff frequency f_{low} , the matched-filter signal-to-noise ratio scales as $\rho \propto f_{\text{low}}^{-2/3}$, since $|h(f)| \propto f^{-7/6}$ in the stationary phase approximation [23]. This scaling amounts to roughly a 60% improvement as the cutoff frequency is halved. On the other hand, the improvement in the amount of early warning for these inspiraling systems can be significant: the time t_{merge} before a coalescing system merges is related (again in the stationary-phase approximation) to the gravitational-wave frequency f_{GW} by $t_{\text{merge}} \propto f_{\text{GW}}^{-8/3}$ [22]. Therefore, sufficiently loud signals will accumulate threshold signal-to-noise ratio soon after entering the sensitivity band, leading to an early warning time $t_{\text{early}} \propto f_{\text{low}}^{-8/3}$. This means that halving the low-frequency cutoff increases the early warning time more than sixfold. Figure 1 shows the accumulation of signal-to-noise ratio ρ found by computing $\rho^2(t_{\text{merge}}) = 4 \int_{f_{\text{low}}}^{f_{\text{GW}}(t_{\text{merge}})} df |h(f)|^2 / S_h(f)$, with $h(f)$ in this

TABLE I. Observational performance metrics for the sensitivities shown in Fig. 2. “BNS” refers to a $1.4 + 1.4 M_{\odot}$ neutron-star system (tidal and postmerger effects not included), and “BBH” refers to a $30 + 30 M_{\odot}$ black hole system, in both cases nonspinning. The time before merger is given for an optimally oriented neutron star system at a redshift $z = 0.03$, with a threshold SNR of 8. M_{\max} is the maximum mass for which an optimally oriented nonspinning equal-mass system could be detected at $z = 1$.

Observatory	$z_{\text{hor}}^{(\text{BNS})}$	$t_{\text{early}}^{(\text{BNS})}$	$z_{\text{hor}}^{(\text{BBH})}$	M_{\max}/M_{\odot}
aLIGO	0.097	12 s	1.2	710
Voyager	0.44	4 min	7.4	950
CE1	4.1	65 min	34	2200
CE2	11	90 min	41	2400
ET	3.6	5 h	57	4000

case chosen to correspond with a $1.4 + 1.4 M_{\odot}$ binary system at $z = 0.03$ (luminosity distance 0.14 Gpc). By setting a threshold SNR of 8, the corresponding early warning time can be solved for and is given in Table I for the detector sensitivities shown in Fig. 2.

Low-frequency sensitivity is especially impactful for the detection of intermediate-mass black holes in the range $100 M_{\odot} \lesssim M \lesssim 1000 M_{\odot}$. Detecting these systems at redshifts approaching 10 would provide information on the oldest population of stars (population III). Additionally, these detections could demonstrate that supermassive black

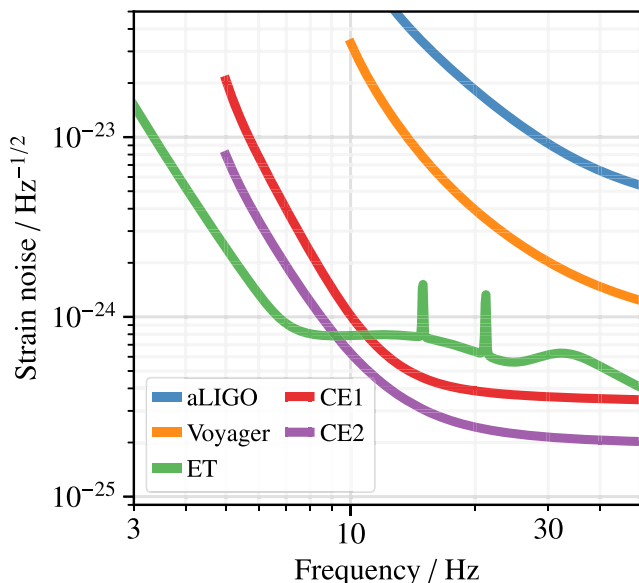


FIG. 2. Strain noise of Advanced LIGO, LIGO Voyager, the six-interferometer Einstein Telescope, and both stages of Cosmic Explorer. In all cases the source is assumed to be circularly polarized. aLIGO and Voyager are shown for $f \geq 10$ Hz, CE for $f \geq 5$ Hz, and ET for $f \geq 3$ Hz; these are the low-frequency cutoffs assumed for the signal calculations throughout this work.

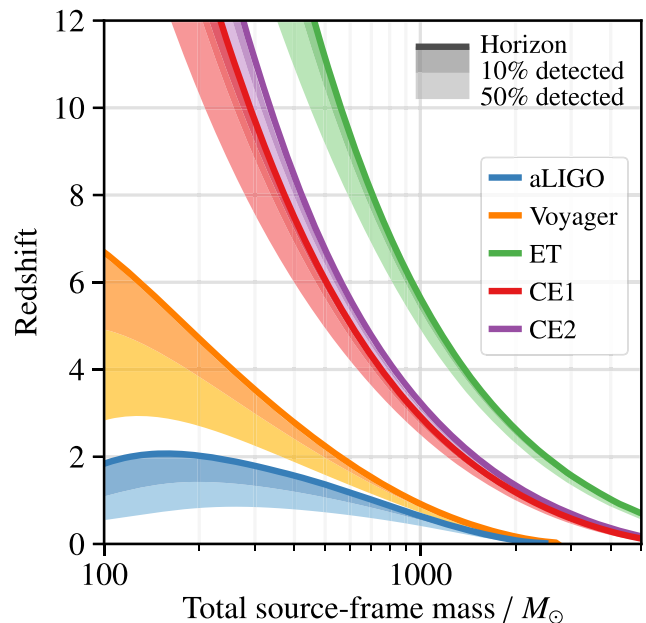


FIG. 3. Detectability of nonspinning equal-mass black hole binaries as a function of mass and redshift, with detectability being defined as having a matched-filter SNR ≥ 8 . The solid line indicates each detector’s horizon, at which an optimally oriented system with a given mass and redshift will be detected with SNR = 8, and suboptimally oriented systems have SNR < 8 . Systems lying above the solid line are limited to SNR < 8 regardless of orientation. Along the edge of the dark (light) shaded band, 10% (50%) of the systems will be detected with SNR ≥ 8 and the remainder will have SNR < 8 due to unfavorable orientation.

holes—approaching and exceeding $10^6 M_{\odot}$ —were formed by accretion and hierarchical mergers from population III remnants (the so-called “light seed” scenario) [25]. Figure 3 shows the response distance [26]—the redshift out to which binary black hole systems can be detected—for Cosmic Explorer and other detectors. Computing the response distance for a threshold signal-to-noise ratio ρ_0 requires numerically solving $\rho_0^2 = 4 \int_{f_{\text{low}}}^{\infty} df |h(f; z)|^2 / S_h(f)$ for the corresponding threshold z ; here $h(f; z)$ is the redshifted (i.e., detector-frame) gravitational waveform, which is obtained from the source-frame waveform $h(f)$ by the substitutions¹ $f \mapsto f/(1+z)$, $m_1 \mapsto (1+z)m_1$, and $m_2 \mapsto (1+z)m_2$ [27]. Table I summarizes the detection prospects for high-redshift, intermediate-mass black hole mergers.

¹These scalings are valid if the detector does not significantly move, due to the Earth’s rotation and orbit around the Sun, while the signal is in that detector’s sensitivity band. This approximation is valid for Cosmic Explorer, since f_{low} is sufficiently high, but not for spaced-based detectors such as the Laser Interferometer Space Antenna.

III. STRAIN SENSITIVITY

Our Cosmic Explorer models adopt the dual-recycled Fabry-Perot Michelson interferometer topology now employed by advanced detectors shown in Fig. 4. In brief, these detectors are Michelson interferometers whose arms are enhanced by the inclusion of partially transmissive input mirrors, turning the arms into Fabry-Perot cavities. Then, a power-recycling mirror is placed between the laser and the beam splitter to critically couple the Fabry-Perot arms to the laser, which maximizes the circulating arm power. Additionally, a signal extraction mirror between the beam splitter and the output port is used to broaden the bandwidth of the instrument [28]. Squeezed vacuum states are reflected off of a filter cavity and injected into the antisymmetric port of the interferometer in order to achieve broadband quantum noise reduction.

The upper limit to the achievable bandwidth of Cosmic Explorer is defined by the free spectral range of the $L = 40$ km arms, given by $f_{\text{FSR}} = c/2L = 3.75$ kHz. We take the lower limit to be 5 Hz; this is not a precisely motivated cutoff, but comes from our expectation of significant noise from local gravity fluctuations at a few hertz from the atmosphere and (if Advanced-LIGO-like suspensions are used) from thermal, seismic, and control noise. The rest of the present work is concerned primarily with the geophysical and thermal noises, leaving a detailed discussion of other noises to later works.

Since the initial exploration of the Cosmic Explorer sensitivity [17], many of the estimates of the fundamental noises have been refined, and some new noise sources have

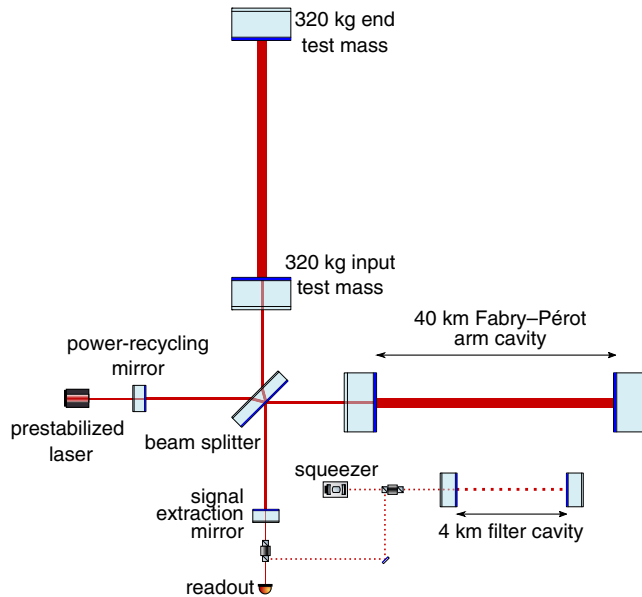


FIG. 4. Simplified Cosmic Explorer interferometer topology consisting of a dual-recycled Fabry-Perot Michelson interferometer in addition to a squeezer and filter cavity used to achieve broadband quantum noise reduction.

been considered. Figures 5 and 6 show the updated low-frequency limits to the spectral sensitivity for CE1 and CE2, respectively, and some of the key sources of noise that contribute to these limits; the curves from the previous sensitivity study are also included. For CE1, updates with respect to previous work mean that the instrument attains strain noise better than 10^{-23} $\text{Hz}^{-1/2}$ above about 5.7 Hz, whereas the instrument presented in previous work attained this performance only above 8 Hz. For CE2, strain noise below 10^{-23} $\text{Hz}^{-1/2}$ is achieved around 4.8 Hz compared to 6.3 Hz in previous work; additionally, the noise performance around 10 Hz is slightly degraded for CE2. The primary differences from this initial work are as follows.

- (i) The ground motion of the Cosmic Explorer facility is assumed to be lower than the LIGO facilities above 5 Hz, based on long-term seismic surveys from some promising locations around the U.S. (Sec. IV). This lowers both the seismic noise and the seismic component of the Rayleigh-wave Newtonian noise.
- (ii) CE1 assumes tenfold better seismic isolation than Advanced LIGO at 1 Hz, and CE2 assumes 100-fold better seismic isolation than Advanced LIGO at 1 Hz (Sec. V B).

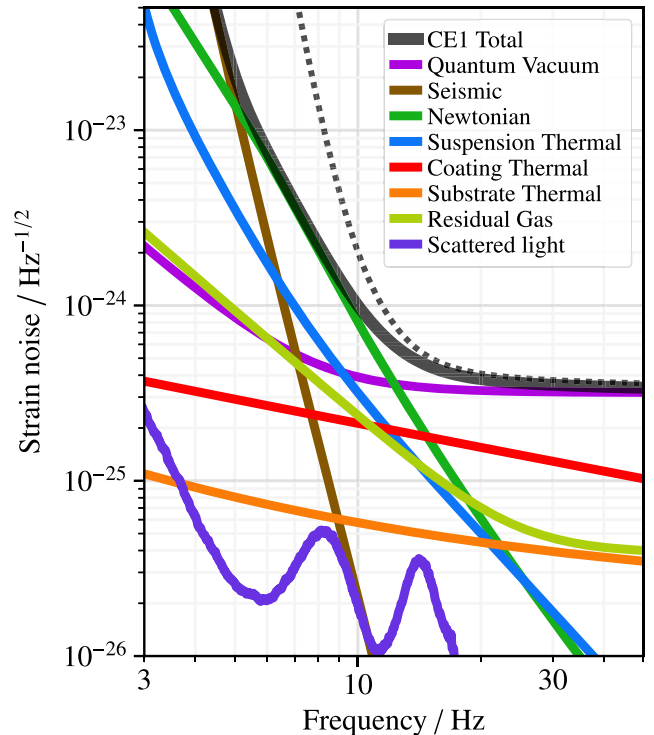


FIG. 5. Estimated low-frequency spectral sensitivity limit (solid black) of Cosmic Explorer 1 and the known noise sources that cause these limits (colored curves). The sensitivity limit from previous work [17] is also shown (dotted black curve). From 5 to 10 Hz, the strain sensitivity is limited by seismic Newtonian noise.

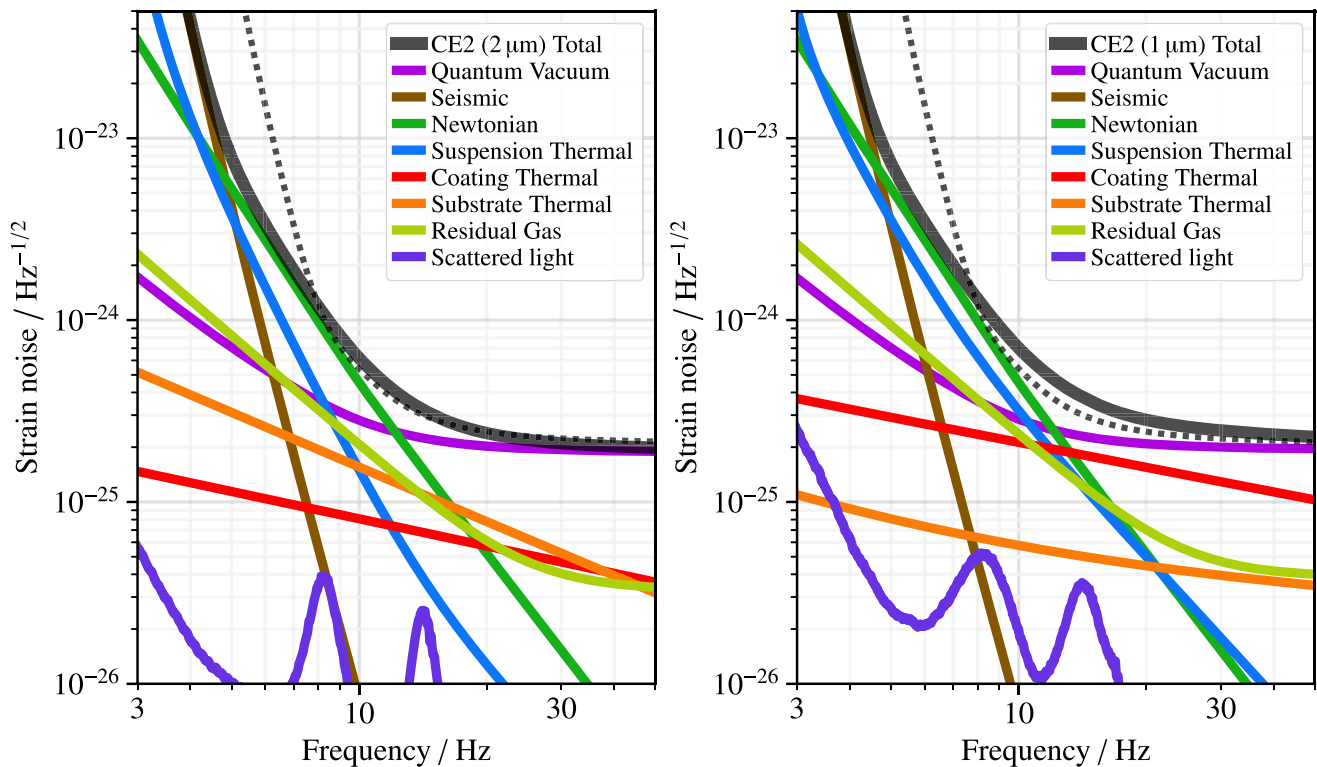


FIG. 6. Same as Fig. 5 but for Cosmic Explorer 2 realized with (left) the $2\ \mu\text{m}$ technology (cryogenic silicon test masses and a $2\ \mu\text{m}$ laser wavelength) and (right) the $1\ \mu\text{m}$ technology (room-temperature fused silica test masses and a $1\ \mu\text{m}$ laser). For both technologies, the seismic and suspension thermal noises are comparable to the infrasonic Newtonian noise background, which is taken to be a geophysical limit for the facility (Sec. V C 2).

- (iii) The Newtonian noise estimates now include contributions from seismic body waves and atmospheric infrasound (Sec. V C), and CE1 assumes twofold suppression of ambient Rayleigh waves. Together with the reassessment of the ground motion, we find that suppression of Rayleigh and body waves is needed for CE2 to meet the sensitivity quoted in [17].
- (iv) Phase noise induced by light propagation in the bulk of the input test masses is now included; this constitutes a potentially non-negligible noise source for the CE2 $2\ \mu\text{m}$ technology (Sec. V D).
- (v) The force noise caused by the residual gas molecules in the test mass chambers striking the test masses is now included (Sec. V F).
- (vi) The possibility of building a room-temperature CE2 with $1\ \mu\text{m}$ technology was not previously considered. Such a detector would have non-negligible coating thermal noise around 10 Hz and thus slightly worse performance than the $2\ \mu\text{m}$ technology and the estimate from previous work at these frequencies (Sec. V D).
- (vii) The suspensions for both detectors have been enlarged to 4 m of total height (previously they

were 3.2 m) and 1500 kg of total mass (previously they were 980 kg) and optimized for minimal thermal and seismic noise given updated mechanical constraints on the strength of the materials (Sec. V A).

- (viii) Preliminary considerations of the scattered-light noise (Sec. V G) and control system noise (Sec. V H) suggest that these noises can be rendered subdominant within the gravitational-wave band.

IV. THE COSMIC EXPLORER FACILITY

Many of the limits to Cosmic Explorer sensitivity at low frequency depend on assumptions about the Cosmic Explorer facility and environment. In this section we lay down requirements for the ground motion and seismic wave content (Sec. IV A), the atmospheric infrasound spectrum (Sec. IV B), and the ultrahigh vacuum system (Sec. IV C). This list is not exhaustive; for example, magnetic requirements are not discussed because the coupling of local magnetic fields depends primarily on technical details of the detector's electronics, which are difficult to estimate without detailed modeling. Similar topics are being considered for the underground Einstein Telescope facility [29].

A. Ground motion

Ground motion limits the performance of gravitational-wave interferometers both through the mechanical coupling from the ground to the suspension point of the test mass and through the direct gravitational attraction of the ground on the test mass (the so-called “Newtonian noise”) [30]. Additionally, ground motion transferred to the beam tube can cause noise from stray light.

The location of Cosmic Explorer is not yet known, but an assumption for the local ground seismicity can be made based on publicly available seismic data and on the noise environment from existing facilities. To get long-term trends that encompass diurnal and seasonal variations in ground motion, we examined noise histograms from selected USArray [31] and Advanced National Seismic System [32] stations in the western U.S.; these stations were chosen for their proximity to promising Cosmic Explorer candidate sites which have favorable topographic properties. We also examined noise histograms from the LIGO Hanford and Livingston sites. Above a few hertz, the ground motion of the LIGO sites is dominated by on-site machinery. In particular, heating, ventilation, and air conditioning systems dominate from 1 to 10 Hz [33]. We assume that it will be possible to design the Cosmic Explorer infrastructure to better isolate the interferometer from such machinery by moving the vibration sources out of the experimental buildings, putting them on dampers or on pedestals mounted separately and deeply into the ground. The Cosmic Explorer ground noise model is shown in Fig. 7; this model assumes that, above 5 Hz, the ground acceleration noise is no more than $1 \mu\text{m s}^{-2} \text{Hz}^{-2}$.

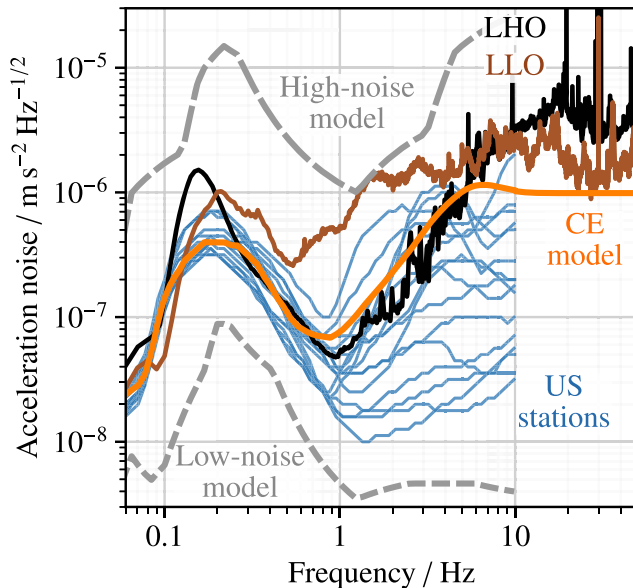


FIG. 7. Model for Cosmic Explorer ground motion, along with representative data from LIGO Hanford (LHO), LIGO Livingston (LLO), and multiyear data from selected seismic stations in the U.S. The Peterson high- and low-noise seismic models are also shown [34].

A complete estimate of the Newtonian noise requires a model of the seismic wave amplitude spectra and an understanding of their propagation through the ground. In general, surface seismic motion is usually assumed to be dominated by surface waves (Rayleigh and Love waves) as opposed to body waves (P and S waves), although the actual composition depends on the particular site and may additionally include higher-order surface waves [35]. Because the Cosmic Explorer site is not known, we adopt a model in which the site is Rayleigh-wave dominated above 5 Hz, with a flat body-wave spectrum of amplitude $0.3 \mu\text{m s}^{-1} \text{Hz}^{-1/2}$ composed equally of P waves, vertically polarized S waves, and horizontally polarized S waves.² Newtonian noise is generated from only the Rayleigh, P, and vertically polarized S waves, because these waves either cause a vertical displacement of the ground surface or density fluctuations of the bulk. The P-, S-, and Rayleigh-wave speeds are assumed to be $c_P = 600 \text{ m/s}$, $c_S = 300 \text{ m/s}$, $c_R = 250 \text{ m/s}$, respectively. These parameters, and the assumptions on the wave content of the ground motion, will have to be revised once the future Cosmic Explorer site is selected and characterized.

B. Atmospheric fluctuations

Newtonian noise from density fluctuations in the atmosphere is likely to impact the strain sensitivity of third-generation detectors. For Cosmic Explorer, the relevant mechanism is expected to be the propagation of infrasound (sound at frequency $f \lesssim 20 \text{ Hz}$) in the vicinity of the test masses. Global infrasound surveys provide noise histograms up to slightly below 10 Hz [36]; based on the median noise model, we take the outdoor infrasound spectrum for Cosmic Explorer to be $1 \text{ mPa Hz}^{-1/2}$. The choice of the median infrasound background means that, while it may be possible to find a site with lower infrasound background, we are not reliant on finding an exceptional site in order to realize the noise performance described herein. The impact of atmospheric infrasound on the detector strain sensitivity is discussed in Sec. V C 2.

Other mechanisms of atmospheric noise generation include spatially varying temperature fields that move near the test mass due to wind and pressure fluctuations generated by turbulent mixing (the aeroacoustic effect), but these noise sources are unlikely to be significant above 5 Hz [30]. Finally, details of the dimension and shape of the buildings housing the test masses can alter the above noise sources (e.g., by excluding large density fluctuations close to the test masses), but have the potential to introduce extra noise due to local vortices [37]. We do not consider details of the test mass buildings here, but note that proper design

²Love waves are not considered because they do not occur in a homogeneous and isotropic elastic half-space; moreover, Love waves do not produce Newtonian noise because their motion is a horizontal shear.

will be needed to ensure that atmospherically induced noise is kept to a minimum. Accurately modeling the Newtonian noise contribution below 5 Hz is an area of ongoing research, and we do not attempt a detailed noise analysis in this frequency band.

C. Vacuum system

The design of the Cosmic Explorer vacuum system, including the beam tube infrastructure and test mass chambers, has not been determined. However, in Sec. V G we determine that a beam tube diameter of 120 cm with a similar acceleration spectrum as the LIGO beam tube motion is likely sufficient to keep noise from backscattered light well below the total Cosmic Explorer noise, though this will be reevaluated once forward-scattering effects are accounted for.

Although the beam tubes and test mass chambers are evacuated, the small amount of residual gas causes noise in the detector through two mechanisms discussed in Sec. V F. The first is optical path length fluctuation due to the polarizability of the molecules in the beam tubes passing through the laser beam [38,39], and the second is test mass motion due to momentum transfer from the gas molecules in the chambers [40,41]. Achieving low pressures is more challenging in the chambers than in the beam tubes because the chambers will be periodically opened in order to make modifications to the detector. We thus set the vacuum system requirements such that the total residual gas noise for the 1 μm technology is a factor of 3 below the CE2 design sensitivity at 10 Hz and a factor of 5 below the design sensitivity at 100 Hz.

In this work we assume that the total vacuum pressure in both the tubes and chambers is dominated by molecular hydrogen, water, molecular nitrogen, and molecular oxygen with each species contributing equally to the total gas noise. Under these assumptions, the above noise requirements translate into requirements on the partial pressures in the beam tubes of $P_{\text{H}_2} = 44$, $P_{\text{H}_2\text{O}} = 4.0$, $P_{\text{N}_2} = 2.5$, and $P_{\text{O}_2} = 2.8$ nPa, for hydrogen, water, nitrogen, and oxygen, respectively, and on the partial pressures in the test mass chambers of $P_{\text{H}_2} = 410$, $P_{\text{H}_2\text{O}} = 140$, $P_{\text{N}_2} = 110$, and $P_{\text{O}_2} = 100$ nPa. It is also important that the hydrocarbons are kept low enough that they do not contaminate the mirror surface and cause excess optical loss.

V. NOISE ESTIMATES

This section describes noise terms that contribute to the limit of the low-frequency performance of Cosmic Explorer.

A. Suspension thermal noise

The baseline Cosmic Explorer design assumes scaled-up versions of the quadruple pendulum suspensions used in LIGO [42] and planned for Voyager [12], along with a few

modifications, to decrease the seismic and suspension thermal noises. The left panel of Fig. 8 shows a diagram of the LIGO suspensions. Suspension thermal noise is related to the mechanical response of the suspensions through the fluctuation dissipation theorem [43–46] as $S(f) \propto T \text{Im}\chi/f$, where χ is the mechanical susceptibility.

In order to minimize thermal noise, the final suspension stage—consisting of the penultimate mass (PUM), the test mass, and the fibers or ribbons between them—is monolithic; for the 1 μm technology, the material is room-temperature fused silica, and for 2 μm technology, the material is cryogenic silicon. The top two masses, called the top mass and the antepenultimate mass (APM), are room-temperature maraging steel for both wavelengths. In order to lower the vertical suspension resonances, the top three stages are suspended by steel wires from steel blade springs attached to the stage above.

In order to further reduce the resonances, the test masses are suspended by a final set of blade springs attached to the PUM made from the same material as the PUM and test mass. One concept for the design of this final stage is shown in the right panel of Fig. 8. The stress and spring

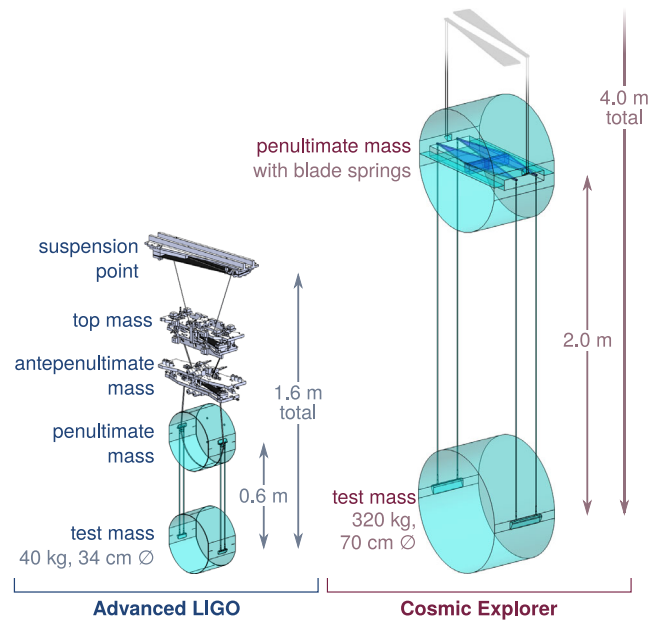


FIG. 8. Left: schematic of the Advanced LIGO quadruple suspensions. Right: one design concept for the final two stages of a Cosmic Explorer silica suspension for a 70 cm diameter fused silica test mass. The components shown in blue are fused silica. In particular, the test masses, PUMs, and fibers between the two are fused silica as are the blade springs on the CE PUM. The components shown in black are maraging steel blade springs. The components shown in silver are the other steel components on the LIGO suspensions. The silicon CE suspensions have silicon ribbons, silicon blade springs on the PUM, and a 80 cm diameter test mass. Note that only the final two stages of the CE suspensions are shown; the full suspension would be similar to LIGO's but would have 4 m total length rather than 1.65 m.

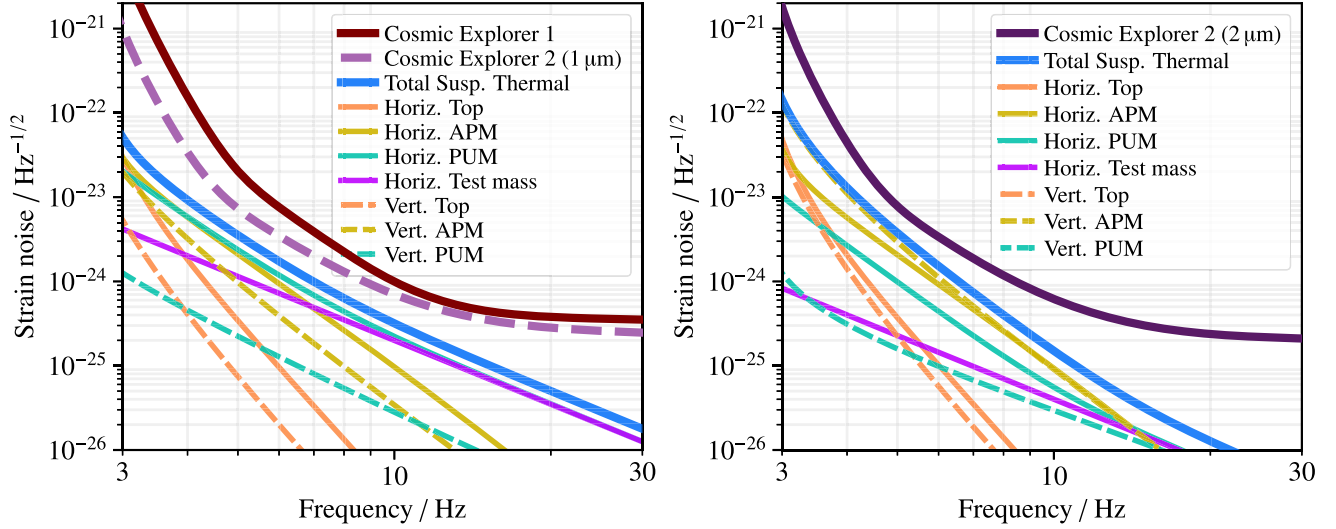


FIG. 9. Contribution of each stage of the test mass quadruple suspension to the total suspension thermal noise for the $1\ \mu\text{m}$ technology (left), which would be common for CE1 and CE2, and for the $2\ \mu\text{m}$ technology (right).

constant of the blade can be calculated with beam theory [47] by approximating it as a rectangular cantilever of length ℓ , width w , and thickness h . The maximum stress $\sigma_{\text{max}} \propto \ell/wh^2$ occurs at the clamp, and the spring constant $k \propto wh^3/\ell^3$ is the ratio of the load suspended by the blade to its maximum deflection at the tip. The blade dimensions should be chosen to minimize k while keeping the maximum stress below a safety factor of the breaking stress of the blade.

For the $1\ \mu\text{m}$ technology, as with LIGO, the silica test mass is suspended from the PUM by four silica fibers welded to the test mass [42]; in Cosmic Explorer they are welded at the top to the blade springs, while in LIGO they are welded directly to the PUM. The contribution of the loss angle ϕ to the imaginary part of the horizontal spring constant $\text{Im}k \propto \phi/D$ is reduced by the dilution factor $D \propto I^{-1/2}$, where I is the cross-sectional area moment of inertia of the fiber or ribbon [46,48,49]. Since $I \propto r^4$ for a fiber of radius r , it is advantageous to make the radius as small as the breaking stress of the fiber allows. Maximizing the stress in the fiber in this way has the added benefit of reducing the contribution of the fiber to the vertical spring constant and increasing the frequency of the first violin mode, which is proportional to $\sigma^{1/2}$.

The thermoelastic noise of the fiber has two contributions: one from thermal expansion and one from the temperature dependence of the Young's modulus. These two contributions cancel when the fiber stress is appropriately chosen. Thus, a tapered fiber is used with a larger radius at the ends (where the most bending, and therefore the most loss, occurs), chosen to give the stress necessary to cancel the thermoelastic noise, and a smaller radius along the length of the fiber is chosen to maximize the stress [42].

For the $2\ \mu\text{m}$ technology, as with Voyager, the silicon test mass is suspended by four silicon ribbons welded to the test mass at the bottom and to the blade springs at the top. Since the ribbons are held near the zero crossing of the thermal-expansion coefficient, the thermoelastic noise in the ribbons cannot be canceled by choice of stress as is done for the fused silica fibers. The ribbon dimensions are therefore chosen to maximize the stress along the entire length of the ribbon. Since $I \propto wh^3$ for a ribbon of width w and thickness h , a width-to-thickness ratio of 10:1 is chosen to soften the pendulum in the horizontal direction and to increase the gravitational dilution.

The suspension design also determines the seismic noise, discussed below in Sec. VB, since the suspensions provide passive $1/f^8$ filtering of seismic noise above all of the longitudinal, vertical, and angular resonances. To reduce both seismic and suspension thermal noise, it is thus advantageous to make the suspensions as soft as possible and to lower their resonances.

To achieve this goal, the total allowable height of the suspensions for all technologies has been increased to 4 m and the total mass increased to 1500 kg. Within these constraints, in an analysis similar to that done for Voyager [12], the lengths and masses of the silica and silicon suspension stages have been optimized to minimize the sum of these noises over the frequency band of 4–15 Hz.

Figure 9 shows the contributions of each stage to the total suspension thermal noise. The silica suspensions are dominated by the horizontal noise of the PUM and test mass above about 10 Hz with contributions from the horizontal noise of the APM below. The silicon suspensions are dominated by vertical noise of the APM below about 7 Hz, above which the horizontal and vertical noises

of the PUM and test mass also start to become important. The addition of blade springs lowers the first vertical mode, thus reducing the vertical thermal noises, most importantly from the APM.

The maximum stress that the blade springs, fibers, and ribbons can tolerate is an important material property in the design of the suspensions, and it is difficult to predict what will be possible on a timescale of decades. The maximum stress of the LIGO silica fibers is 800 MPa [42], which provides a safety factor of about 6 for the breaking stress of fibers realized at the time the LIGO suspensions were designed [50]. Recent improvements to fused silica fiber fabrication suggest that fibers can be made with stresses of 1.2 GPa, which provides a safety factor of about 3 [51]. The Cosmic Explorer fused silica suspensions use this 1.2 GPa for the fibers and tentatively set the maximum blade spring stress to be 800 MPa.

The silicon studies most relevant to the suspensions discussed in this section find that the tensile strength depends on the surface treatment and edge quality, with average breaking stresses measured ranging from 100 to 400 MPa and individual samples observed as high as 700 MPa [51,52]. Cosmic Explorer tentatively sets a maximum stress of 400 MPa for both the blades and ribbons, while Voyager uses a more conservative 100 MPa [12]. Nevertheless, larger stresses have been observed in other contexts. Stresses of 3–5 GPa have been observed in silicon wafers [53] and microscale MEMS devices have realized fracture stresses in excess of 1 GPa and stresses of up to 10 GPa have been realized in nanoscale devices [54].

No blade springs have yet been constructed out of either silica or silicon. Developing this technology and techniques for manufacturing highly stressed materials is a critical area of research and development in realizing the low-frequency sensitivity of Cosmic Explorer. Alternatives to blades springs, such as geometric antisprings [55], should also be developed in parallel. Additionally, no experiment on Earth has ever directly measured (low) suspension thermal noise.

B. Seismic noise

Like Advanced LIGO [42,56], Cosmic Explorer will suppress seismic noise with passive and active techniques. The suspensions described in Sec. VA passively filter the seismic noise with a $1/f^8$ slope in amplitude above the suspension resonances, which have been reduced with the optimization described there. Even so, in order to achieve the required seismic noise suppression, the motion of the optical table supporting the suspension will be actively suppressed with a combination of inertial sensors and position sensors. The seismic isolation of the Cosmic Explorer 1 and 2 suspension point is shown in Fig. 10.

For CE1, we assume an isolation performance that is moderately improved compared to Advanced LIGO [56]. At ~ 10 Hz we assume a threefold improvement, and at

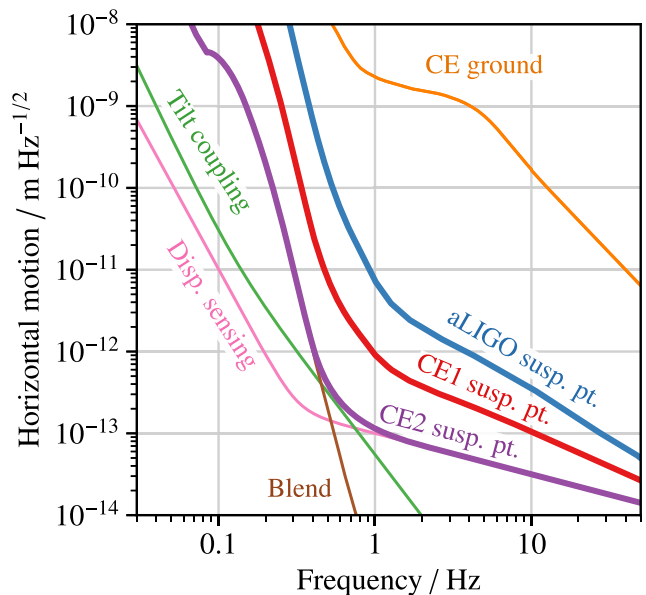


FIG. 10. Horizontal motion of the Cosmic Explorer suspension point, shown for both CE1 and CE2. CE1 assumes seismic isolation that is moderately improved compared to Advanced LIGO. CE2 assumes further improvements to the seismic isolation using novel inertial sensing technology [57]. A simplified budget of the CE2 motion is also shown, along with the CE ground motion model (Fig. 7).

~ 1 Hz a tenfold improvement, though to directly increase the seismic isolation the improvement is only needed down to 5 Hz; seismic isolation improvements below the gravitational-wave band will, however, lessen the requirements on the interferometer control system. The improvement could come, for example, by combining the mechanics of a conventional geophone (GS13) with an interferometric proof mass readout [58]. The noise below 1 Hz is residual ground motion that comes from the inclusion of a position sensor signal to lock the suspension point to the ground on long timescales (also referred to as “blending”). Additionally, the horizontal inertial sensing is susceptible to contamination from ground tilt and should therefore be paired with low-noise tiltmeters [59]. This is motivated by studies at LIGO Hanford that have shown significant tilt-to-interferometer strain coupling after active seismic isolation [60].³

For CE2, we assume that improvements in inertial sensing will yield another threefold noise improvement at 10 Hz and a tenfold improvement at 1 Hz, again with the improvement only needed down to 5 Hz to achieve a direct seismic isolation improvement. A variety of designs have been proposed, but common themes include a monolithic proof mass assembly to reduce thermal noise and an optical

³Lowering the tilt coupling, along with mitigating gravity-gradient fluctuations from the atmosphere, is an important motivator for carefully designed buildings [61].

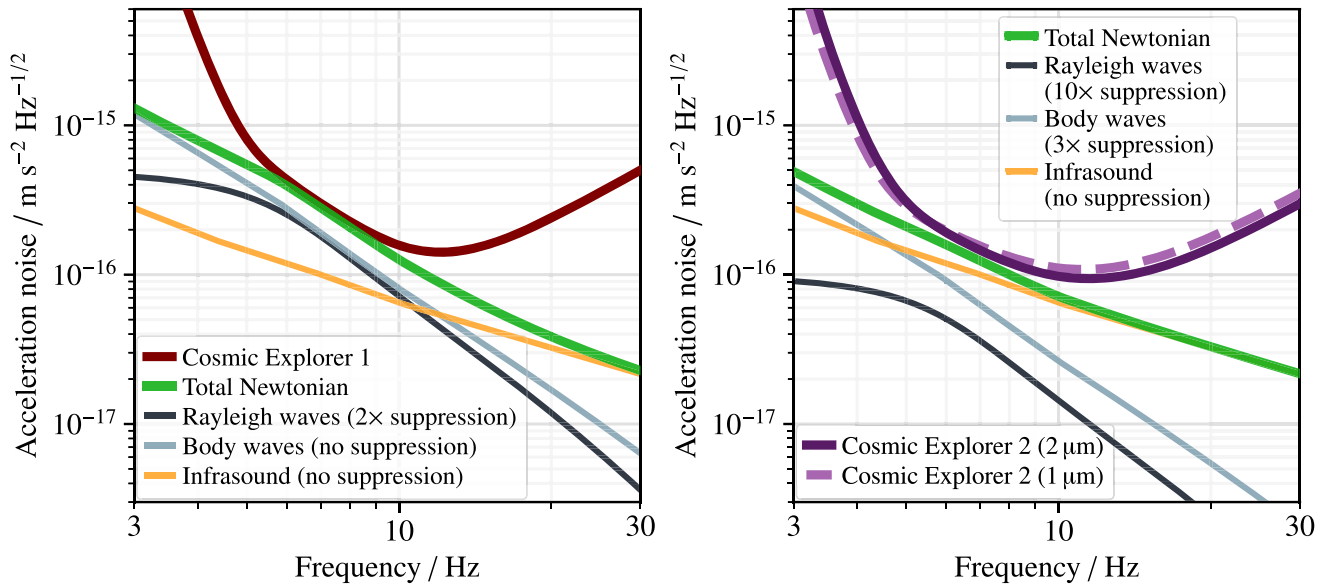


FIG. 11. Newtonian noise estimates for Cosmic Explorer. For CE1, the Rayleigh-wave content is assumed to be suppressed by a factor of 2 in amplitude below the ground motion shown in Fig. 7, either through off-line subtraction or local mitigation (e.g., excavation as described in Sec. V C 3) in the immediate vicinity of the test mass. The P- and S-wave amplitudes are each assumed to be a factor of 10 higher than the Peterson low-noise model [34]. For CE2, the Rayleigh-wave content is assumed to be suppressed by a factor of 10 in amplitude, and the body-wave content is suppressed by a factor of 3 in amplitude. The infrasound amplitude is taken from the Bowman model [36].

displacement sensor to reduce readout noise. Van Heijningen *et al.* demonstrated a monolithic accelerometer combined with an interferometric readout that reached a noise floor of $8 \times 10^{-15} \text{ m Hz}^{-1/2}$ above 30 Hz; this should reach $10^{-15} \text{ m Hz}^{-1/2}$ above 10 Hz with continued development [62]. A proposed superconducting niobium upgrade to this system would reduce eddy current damping and greatly improve suspension thermal noise allowing, in principle, $10^{-15} \text{ m Hz}^{-1/2}$ above 1 Hz [63]. However, such a device has yet to be demonstrated and would operate at temperatures below 9.2 K, requiring additional cooling with respect to the Cosmic Explorer cryogenic environment, and would require a low-noise tiltmeter. Development of novel six-dimensional inertial isolators with optical readouts is also progressing [57], and their use with the existing LIGO facilities and Advanced LIGO isolation infrastructure has been explored [64]. These sensors would provide the additional benefit of sensing tilt. Additionally, the improved low-frequency noise of the inertial sensors leads to less reliance on the low-frequency position sensor signal, thereby lessening the contamination from residual ground motion.

C. Newtonian noise

Previous studies of Newtonian noise for Cosmic Explorer considered only the contribution from seismic Rayleigh waves and assumed a Rayleigh-wave noise amplitude equal to that of the existing LIGO facilities [17]. Here we refine that estimate and additionally include

the contributions from seismic body waves and from atmospheric infrasound. We start with analytical formulas available in the literature for the infinite half-space, and then additionally we consider numerical simulations that account for trenches that can reduce Newtonian noise relative to the half-space solutions. The Newtonian noise estimates are shown in Fig. 11.

1. Seismic Newtonian noise

As described in Sec. IV A, we assume that, compared to LIGO, the Cosmic Explorer facility will have a lower Rayleigh-wave noise in the anthropogenic band: $1 \mu\text{m s}^{-2} \text{ Hz}^{-1/2}$ above 5 Hz. We also assume a body-wave noise amplitude equal to $0.3 \mu\text{m s}^{-2} \text{ Hz}^{-1/2}$ above 5 Hz, equipartitioned among P waves, vertically polarized S waves, and horizontally polarized S waves.

To compute the Newtonian noise from seismic and infrasonic density fluctuations, we employ the formulas from Harms [30], which are valid for a test mass suspended above a homogeneous, isotropic elastic half-space. We therefore do not consider effect of stratigraphy, other ground anisotropies, the interaction with structures, or the interconversion of different types of seismic waves. These features will need to be accounted for to get a full understanding of the behavior of the local seismic field and hence the Newtonian noise level. For CE1, we have assumed that the effect of seismic Newtonian noise can be mitigated (Sec. V C 3) with 2x amplitude suppression of Rayleigh waves. The result in Fig. 11 shows that CE1 is

limited by seismic Newtonian noise from 5 to 10 Hz, with a secondary contribution from infrasound. For CE2, we have assumed that seismic Newtonian noise can be further mitigated with 10x amplitude suppression for Rayleigh waves and 3x amplitude suppression for body waves; the result in Fig. 11 shows that CE2 is then limited by atmospheric Newtonian noise, described below.

2. Atmospheric Newtonian noise

As mentioned in Sec. IV B, we assume the Cosmic Explorer facility has a typical infrasound spectrum of $1 \text{ mPa Hz}^{-1/2}$; this is an extrapolation from long-term global infrasound data, available below 10 Hz [36], and assumes no significant contribution from site infrastructure.

To compute the Newtonian noise induced by infrasound fluctuations, we use the calculation in Harms [30], which is valid for a test mass immersed in a fluid half-space. The result is shown in Fig. 11. For both stages of Cosmic Explorer, no suppression is assumed.

As mentioned in Sec. IV B, we do not include other processes besides infrasound that produce density fluctuations in the atmosphere, such as advected temperature fluctuations or aeroacoustic noise, because we expect the Newtonian noise induced by these processes to be negligible above a few hertz.

3. Mitigation strategies

Unlike mechanically coupled seismic and acoustic noise, which can be strongly attenuated by suspending and inertially isolating the test mass inside a vacuum chamber, the Newtonian effect of seismic and acoustic fluctuations cannot be attenuated except by reducing the fluctuation amplitude, increasing the distance from the fluctuations to the test mass, or using auxiliary sensors to estimate the Newtonian contribution to the detector strain channel. Newtonian noise mitigation therefore requires a different set of techniques than for mechanical isolation, and the amount of achievable suppression will not be as great.

CE1 calls for mitigating the seismic Rayleigh-wave Newtonian noise by a factor of 2 in amplitude; CE2 calls for mitigating the seismic Rayleigh-wave Newtonian noise by a factor of 10 in amplitude and the seismic body-wave Newtonian noise by a factor of 3 in amplitude. This mitigation could be achieved by several means, potentially used in concert:

- (1) Seismometer array subtraction. Arrays of seismometers can be used to estimate the seismic field in the vicinity of the test mass and thereby subtract Newtonian noise from the gravitational-wave channel [65]. A proof-of-principle experiment to subtract ground motion from a tiltmeter signal achieved a tenfold suppression in the region 10–20 Hz [60].
- (2) Excavation underneath the test masses. Nearby density and displacement fluctuations can be suppressed simply by removing earth from the vicinity

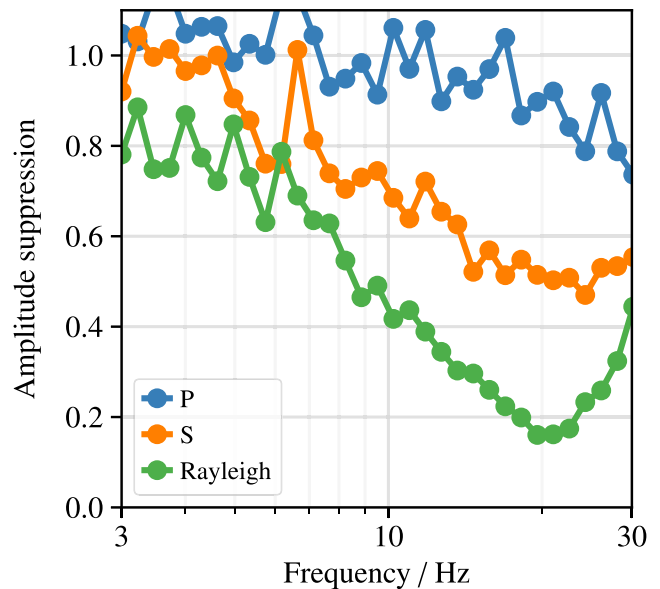


FIG. 12. Seismic Newtonian-noise reduction amplitudes for P, S, and Rayleigh waves achieved by removing ground from underneath the test mass to make an 11 m wide and 4 m deep recess. This reduction estimate is computed using the Born approximation, which may affect the validity of the Rayleigh-wave reduction estimate above 15 Hz [66]; the body-wave reduction estimate should not be significantly affected. The scatter in the curves is due to the finite number of waves simulated and the finite size of the numerical grid.

the test mass, replacing it with a lightweight fill material such as extruded polystyrene if necessary. Harms and Hild [66] computed the suppression of Rayleigh-wave Newtonian noise from a 11 m wide and 4 m deep hemispherical recess, and here we repeat their analysis to additionally include the effect of the recess on P and S waves. The result is shown in Fig. 12, showing that moderate reduction of Rayleigh waves can be achieved near and above 10 Hz, while the reduction of body waves is less significant.

- (3) Topography and seismic metamaterials. Seismic metamaterials could be built to deflect or dissipate seismic waves before they arrive at the test mass, potentially suppressing surface wave amplitudes by a factor of a few [67–72]. Similarly, berms, ditches, and other nearby topographic features can affect the propagation of seismic waves and thus the Newtonian noise level.

No mitigation of infrasound noise is assumed, and thus infrasound is considered a sensitivity limit of the Cosmic Explorer facility. Tropospheric LIDAR, which would otherwise be well suited to three-dimensional estimation of atmospheric fluctuations, would require sensitivity improvements of several orders of magnitude in order to sense and subtract infrasound [73]. Baffling or otherwise

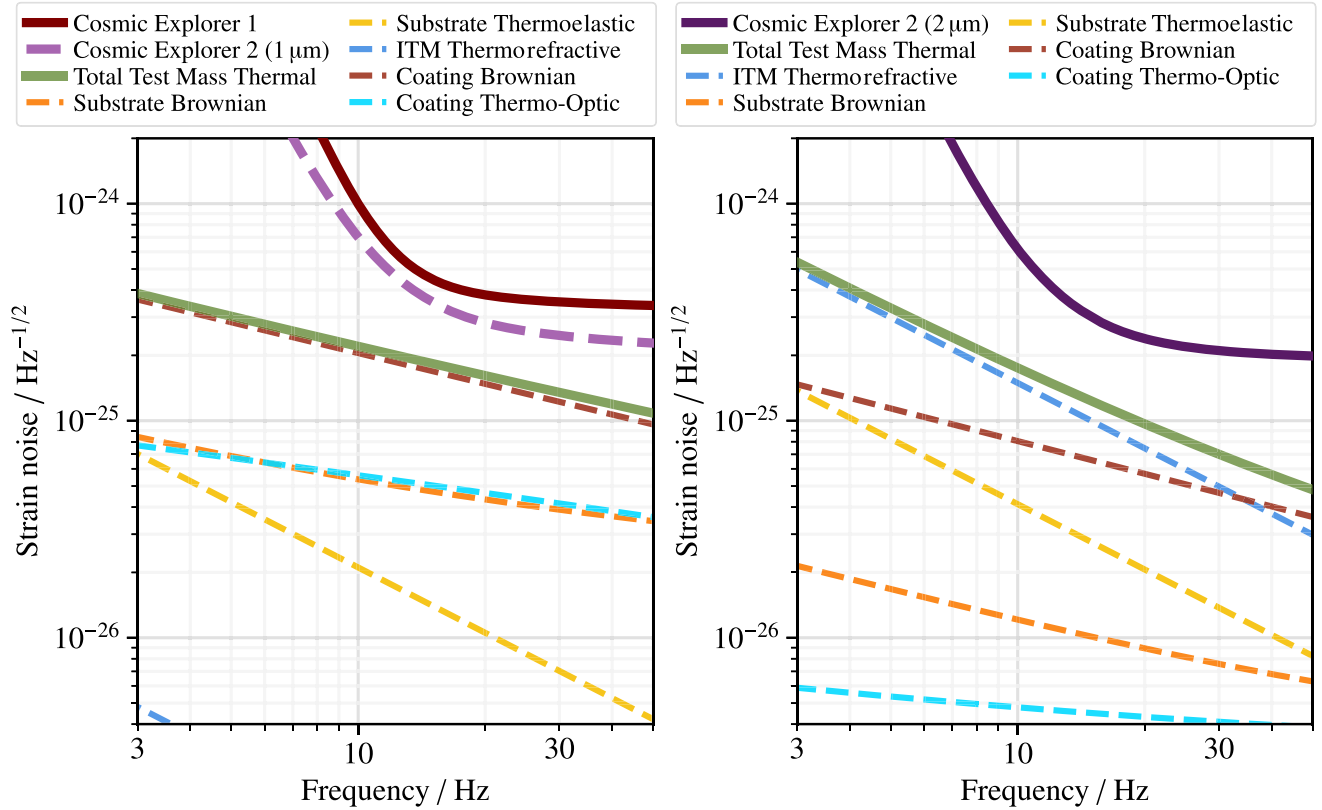


FIG. 13. Thermal noise levels, and individual noise contributions to them, of the test mass substrates and coatings for the $1\ \mu\text{m}$ technology (left), which would be common for CE1 and CE2, and for the $2\ \mu\text{m}$ technology (right).

acoustically isolating the interior of the test mass building may be able to reduce the infrasound Newtonian noise below the outdoor value at a discrete set of frequencies [74]. A true cutoff for infrasound noise could be engineered by burying the test mass a depth d below ground, which would suppress the noise by e^{-df/c_s} , where c_s is the speed of sound; however, to achieve significant suppression for $f \geq 5$ Hz would require $d \geq 65$ m. Additionally, underground operation requires a reassessment of the Newtonian noise, since the detector would operate in the bulk of the ground rather than on the surface.

D. Test mass thermal noise

Cosmic Explorer will use heavy, high-quality test masses which are turned into high-reflectivity Bragg mirrors by coating the test mass surface with multiple layers of dielectric films. By alternating between high- and low-refractive-index materials, and depositing the layers to a thickness that is the same scale as the laser wavelength, the coating creates the conditions for repeated thin-film interference of the laser beam [75]. The performance of the coating depends on the optical, mechanical, and thermal properties of the materials, which therefore must be chosen with some care [76].

The $1\ \mu\text{m}$ coating technology will mostly be that of LIGO A+: room-temperature fused silica substrates and

coating technology being developed for A+ [77]. Current research aimed at improving the thermal noise of room-temperature coatings holds promise to result in improved coatings for A+ and thus the $1\ \mu\text{m}$ CE technology [78]. The $2\ \mu\text{m}$ technology will mostly be that of LIGO Voyager: crystalline silicon substrates operated at 123 K, with coating materials that offer improved thermal noise performance over the $1\ \mu\text{m}$ technology.

Estimated thermal noises associated with the Cosmic Explorer test masses and their coatings are shown in Fig. 13, the relevant parameters are given in Table II, and the individual noises are discussed below. Neither the A+ nor the Voyager coating designs have been finalized, so in this work we have made assumptions about the high- and low-index material pairs. Depending on the progression of coating research in the next decade, it is possible that the coatings for CE1 or CE2 may be different from what is presented here and could potentially use three or more materials to provide more flexibility to simultaneously optimize the optical and thermal noise properties of the mirrors [79,80].

1. Substrates

Cosmic Explorer will use 320 kg test mass substrates; this comes from the desire to make quantum radiation-pressure noise subdominant to other noise sources and the

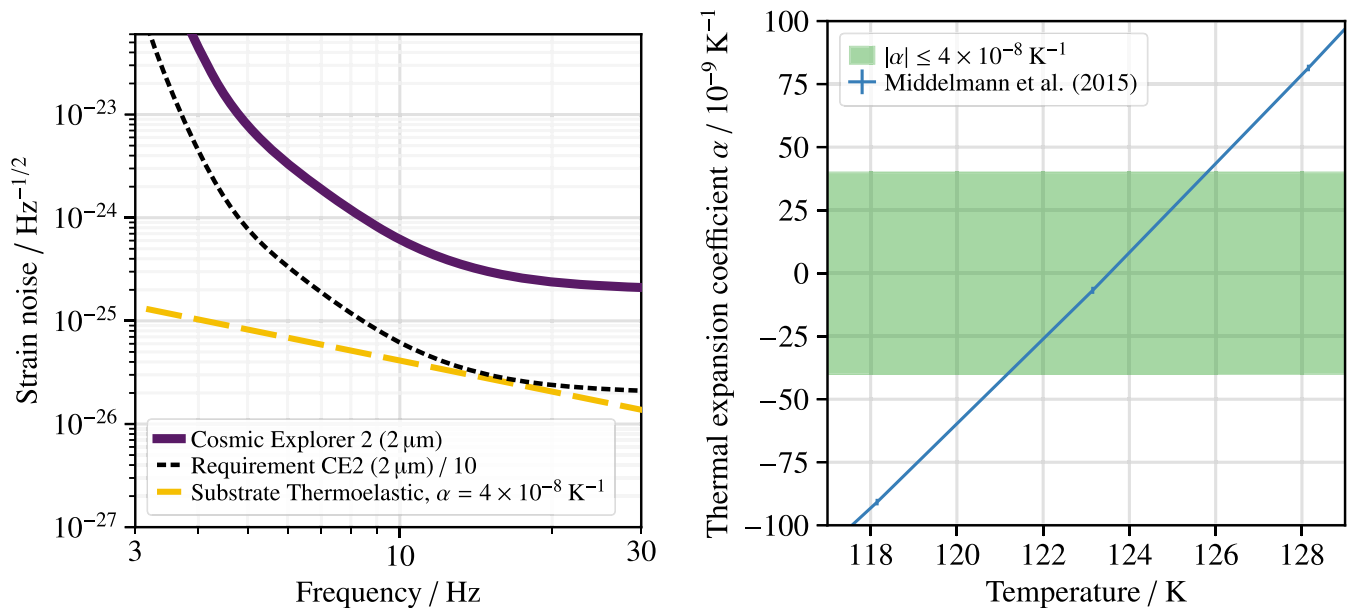


FIG. 14. Left: amplitude spectral sensitivity of CE2 realized by the cryogenic silicon 2 μm technology compared with the estimated thermoelastic noise of the silicon test mass substrates for $\alpha = 4 \times 10^{-8} \text{ K}^{-1}$. The requirement that thermoelastic noise be a factor of 10 below the CE2 design curve is met when $\alpha = \pm 4 \times 10^{-8} \text{ K}^{-1}$. Right: coefficient of thermal expansion of crystalline silicon versus temperature measured by Middelmann *et al.* [85], enlarged to show the data points and error bars around the zero crossing at 123.5 K. The green region indicates the required $|\alpha| \leq 4 \times 10^{-8} \text{ K}^{-1}$, corresponding to a temperature accuracy of about $\pm 2.3 \text{ K}^{-1}$.

necessity of having large test masses to accommodate the large diameter beams of a nearly diffraction limited 40 kg long arm cavity. There are several sources of thermal noise in test mass substrates: mechanical (Brownian) noise, thermoelastic noise, and thermorefractive noise.

Brownian fluctuation causes a displacement of the mirror surface with a power spectrum $S(f) \propto T\phi/wf$, where T is the test mass temperature, w is the spot size of the beam, and ϕ is the mechanical loss of the substrate material; there are order unity corrections due to the finite size of the test mass and additional loss on the test mass surface [81].

Thermoelastic noise is driven by thermodynamic fluctuations that cause displacement of the test masses via the coefficient of thermal expansion α [82]: the spectrum of the test mass surface displacement due to these fluctuations is $S(f) \propto T^2\kappa\alpha^2/w^3f^2$, where κ is the thermal conductivity of the substrate. For fused silica, the contribution of substrate thermoelastic noise to the total instrument noise is negligible. In order to prevent the substrate thermoelastic noise of silicon from making a significant contribution, the substrate temperature must be controlled to near the zero crossing of the thermal-expansion coefficient [12,83]. The left panel of Fig. 14 shows that $|\alpha| \leq 4 \times 10^{-8} \text{ K}^{-1}$ meets the requirement for thermoelastic noise to be an order of magnitude below the total design sensitivity. Based on models [84] and measurements [85] of the temperature dependence of α , this constraint on α translates to a temperature control requirement of $\pm 2.3 \text{ K}$ relative to the zero-crossing temperature of α . This temperature

control accuracy is also sufficient to keep thermoelastic noise of the silicon components of the suspension from contributing significantly to the total low-frequency suspension thermal noise for the 2 μm technology as shown in Fig. 9.

To achieve $\pm 2.3 \text{ K}$ temperature control, it may be sufficient to control the test mass temperatures to a fixed value (for example using the frequency of the internal modes of the silicon test masses as a reference for temperature), or it may be necessary to determine the set temperature based on minimizing the observed noise or by actively measuring the substrates' α values. The sign change of α around the zero crossing allows for a signed error signal that would enable negative feedback control. Typical room temperature variations achieved at the current LIGO observatories are of order $\pm 1 \text{ K}$, and even better accuracy should be achievable with feedback control [83,86]. Temperature gradients due to heating from the environment and from absorbed laser power also need to be considered. If a power P_{abs} is absorbed on some area A of the test mass and dissipates into the substrate, the resulting temperature variation ΔT is determined by Fourier's law, which reads approximately $P_{\text{abs}}/A \sim \kappa\Delta T/Z$, where Z is a relevant length dimension for the test mass (both the thickness and diameter are of similar magnitude for Cosmic Explorer). This suggests that in the case of a few watts of laser power absorbed in the coating (i.e., a coating absorption of roughly 1 ppm), the temperature variation in the substrate should be of order tens of

TABLE II. Requirements for the substrate, coating, and optical properties of the Cosmic Explorer input test masses (ITMs) and end test masses (ETMs). The high-index coating material for the room-temperature technology is still to be determined (TBD), so it has been assumed to have the same properties as the titania-doped tantala used in current detectors, but with a mechanical loss such that the overall coating loss is 4 times lower than the current Advanced LIGO coating loss.

Quantity		1 μm technology	2 μm technology	Remarks
Substrate	Material	Fused silica	Crystalline silicon	
	Temperature T	293 K	123 K	To within ± 2.3 K for CE2
	Diameter	70 cm	80 cm	
	Thickness H	38 cm	27 cm	
	Mass M	320 kg	320 kg	
	Thermal-expansion coefficient α	0.39 ppm K ⁻¹	0.04 ppm K ⁻¹	See remark on T
	Refractive index n	1.45	3.5	
	Thermorefractive coefficient β	9.6 ppm K ⁻¹	100 ppm K ⁻¹	
Thermal conductivity κ	1.38 W m ⁻¹ K ⁻¹	700 W m ⁻¹ K ⁻¹		
Coating	Materials	SiO ₂ /TBD	SiO ₂ /aSi	Low index/high index
	Refractive indices	1.45/2.07	1.44/3.5	
	Loss angles	$2.3 \times 10^{-5}/7 \times 10^{-5}$	$1 \times 10^{-4}/3 \times 10^{-5}$	
	ITM coating layers	16	11	
	ETM coating layers	38	15	
Optical	Vacuum wavelength λ	1 μm	2 μm	
	ITM spot size w_i	12 cm	16 cm	$1/e^2$ intensity radius
	ETM spot size w_e	12 cm	16 cm	
	ITM transmissivity \mathcal{T}_i	1.4%	1.4%	
	ETM transmissivity \mathcal{T}_e	5 ppm	5 ppm	

millikelvins, which is within the ± 2.3 K limit set by the thermoelastic noise coupling.

The same thermal fluctuations that drive thermoelastic noise also cause phase fluctuations in light passing through the substrates, which is relevant for the two input test masses (ITMs). For both silica and cryogenic silicon, this phase fluctuation is dominated by changes in the index of refraction via the thermorefractive coefficient $\beta = dn/dT$ [87–89]. The power spectrum of this noise is $S(f) \propto \kappa T^2 \beta^2 H / \mathcal{F} w^4 f^2$, where H is the thickness of the test mass, $\mathcal{F} \simeq 2\pi / \mathcal{T}_i$ is the finesse of the arm cavities, and \mathcal{T}_i is the transmissivity of the input test masses. For fused silica, this noise is well below the other test mass thermal noises. For cryogenic silicon, the higher thermal conductivity and larger thermorefractive coefficient make this noise non-negligible; with the choice of $\mathcal{F} \simeq 450$, the thermorefractive noise at 10 Hz dominates the total test mass thermal noise for the 2 μm technology⁴ and is similar in magnitude to the coating Brownian thermal noise at 10 Hz for the 1 μm technology.

Additionally, the semiconductor nature of silicon gives rise to refractive index fluctuations due to the motion of free carriers in the silicon test masses. Initial estimates of this

noise source [90] suggested that the phase noise induced by these fluctuations could be significant, but a more recent analysis that includes Debye screening indicates that this noise will lie several orders of magnitude below the total thermal noise of the substrate [91]. We therefore do not consider this noise source.

Finally, we remark on the static birefringence effects in the test mass substrates. Cosmic Explorer, like current gravitational-wave laser interferometers, is designed to operate in a single linear polarization; interconversion of polarization inside the interferometer acts as an optical loss. The greatest potential for polarization interconversion is in the substrates of the input test masses, and consequently the optical gain of the power-recycling cavity could be impacted. Given a mass thickness of H and a birefringence Δn , the power-recycling gain is limited to $G < 1 / \sin^2(\pi \Delta n H / \lambda)$ [92]; maintaining $G = 65$ therefore requires $\Delta n \lesssim 10^{-7}$. This already appears achievable in existing fused silica interferometers and in laboratory measurements of monocrystalline silicon [93]; for the large-diameter masses of Cosmic Explorer, particularly for the silicon technology which has not yet been demonstrated for kilometer-scale instruments, small birefringence must be maintained over a large area, requiring good optical isotropy and control of the stresses in the substrate.

2. Coating noises

As with the test mass substrates, the thin-film coatings applied to the test masses also exhibit thermal

⁴The finesse could be increased to decrease the thermorefractive noise and the power absorbed in the input test mass substrates; however, this value is chosen as a compromise to reduce the effects of signal extraction cavity loss on the high-frequency quantum noise, which favors small \mathcal{F} .

noises that are driven by mechanical and thermodynamic fluctuations.

The 1 μm technology assumes the same target set for the LIGO A+ coatings: an effective factor of 4 overall reduction in mechanical loss compared to the current Advanced LIGO coatings. This will likely be achieved using silica for the low-index layers, and a yet-to-be-determined metal oxide (or set of metal oxides) for the high-index layers. Recent measurements indicate that the loss angle of thin-film silica can be as low as 2.3×10^{-5} [77]; to reach the 4x loss reduction target, this requires a loss angle of the high-index layers of 7.0×10^{-5} . The 2 μm technology assumes LIGO Voyager coatings, where the low-refractive-index layer is again SiO_2 , but the high-refractive-index is now amorphous silicon (aSi) with at most 1 ppm optical absorption [12].

The coating Brownian noise is computed using the formalism of Hong *et al.* [94], with the photoelastic effect ignored and the loss angle in bulk and shear strains assumed to be equal.⁵

As in the substrates, thermodynamic fluctuations produce phase fluctuations of the light propagating in the coatings. The phase fluctuations are mediated by the coating's average coefficients of thermal expansion $\bar{\alpha}_c$ and thermorefractive $\bar{\beta}_c$. Because of the etalon effect, these coefficients act with opposite sign, leading to an overall thermo-optic effect that for most coatings—including the Cosmic Explorer coatings—is smaller than the thermo-elastic or thermorefractive effects individually [95].

E. Quantum noise

The quantum vacuum fluctuations of the modes of the electromagnetic field that enter the antisymmetric port of the interferometer are a significant source of noise at all frequencies [96–98]. Quantum radiation-pressure noise is caused by the laser light in the arm cavities beating with the vacuum fluctuations in the amplitude quadrature of these modes, producing a fluctuating radiation-pressure force acting on the test masses. Shot noise is caused by the beating of the laser with the vacuum fluctuations in the orthogonal phase quadrature, which carries the gravitational-wave strain signal.

It is possible to alter the correlations between the fluctuations in these two quadratures in order to modify the quantum radiation-pressure and shot noises. This is a rich subject which we do not attempt to review here; see, for example, Refs. [99–101] and references therein.

⁵A formula for Brownian noise under these assumptions is given by Eq. (1) of Yam *et al.* [79], but the expression for their coefficient b_j has an error; the corrected expression using their notation is [80]

$$b_j = \frac{1}{1 - \sigma_j} \left[\left(1 - n_j \frac{\partial \phi_c}{\partial \phi_j} \right)^2 \frac{Y_s(1 - \sigma_j - 2\sigma_j^2)}{Y_j(1 - \sigma_s - 2\sigma_s^2)} + \frac{Y_j(1 - \sigma_s - 2\sigma_s^2)}{Y_s(1 + \sigma_j)} \right].$$

We summarize only those aspects strictly relevant to the Cosmic Explorer design outlined in Sec. III. Radiation pressure dominates at low frequencies with a strain power spectral density $S(f) \propto P_{\text{arm}}/\lambda M^2 f^4$. Shot noise dominates at higher frequencies; within the bandwidth of the instrument, the strain power spectral density of the shot noise is $S \propto \lambda/P_{\text{arm}}$, where P_{arm} is the power in the arm cavities and M is the mass of the test masses. The crossover occurs at a frequency $\propto \sqrt{P_{\text{arm}}/M\lambda}$ of about 10 Hz for Cosmic Explorer. The 1 and 2 μm technologies have arm powers of 1.5 and 3 MW, respectively, so both realizations of CE2 have the same level of quantum noise.

Squeezed vacuum states [102,103] can be injected into the antisymmetric port to reduce the noise in one quadrature at the expense of increasing the noise in the orthogonal quadrature, a technique which is being used in Advanced LIGO [104] and Advanced Virgo [105]. Therefore, this necessitates a trade-off between reducing radiation pressure at low frequencies and shot noise at high frequencies. However, the frequency dependence necessary to achieve a broadband noise reduction can be realized by first reflecting the squeezed vacuum off of a detuned optical cavity, known as a filter cavity, before injection into the interferometer [97,106,107]. The production of these frequency-dependent squeezed vacuum states has been realized experimentally [108,109] and will be used in LIGO A+ and Advanced Virgo+.

Cosmic Explorer will employ a 4 km long filter cavity to achieve a broadband quantum noise reduction of 6 dB for CE1 and 10 dB for both realizations of CE2. The filter cavity is critical in achieving the low-frequency goals: without it and with this level of squeezing at mid to high frequencies, CE1 would be limited by radiation pressure down to 10 Hz and CE2 would be limited down to 5 Hz.

F. Residual gas noise

The residual gas in the vacuum system is responsible for two noise sources. The first is a phase noise caused by fluctuations of the gas column density in the beam tubes. The contribution to this noise from a particular molecular species with partial pressure P_{tube} in the tube, mass m , and polarizability α is white up to a cutoff frequency $\propto v_T w_0/L\lambda$, determined by the time it takes for a molecule to cross the laser beam, with a power spectrum $S \propto \alpha^2 m^{1/2} w_0 P_{\text{tube}}/T_{\text{tube}}^{3/2} \lambda$, where T_{tube} is the temperature of the tube, λ is the wavelength, w_0 is the laser beam's waist, L is the length of the arm, and v_T is the thermal velocity of the molecule [38,39].

The second is a force noise caused by the residual gas in the chambers exerting a damping force on the test masses. The contribution of one molecular species with partial pressure P_{chamber} in a chamber to this noise has a power spectrum $S(f) \propto T_{\text{chamber}}^{1/2} m^{1/2} R^2 P_{\text{chamber}}/M^2 f^4$, where M and R are the mass and radius of the test mass, respectively,

and T_{chamber} is the temperature of the chamber [40,41]. The magnitude of these two noise sources determine the pressure requirements in the beam tubes and test mass chambers for each gas species described in Sec. IV C.

G. Scattered-light noise

Scattering of light within the beam tubes is a source of noise for all ground-based interferometric gravitational-wave detectors, as first calculated by Thorne [110]. Imperfections on the surface of the test masses lead to scattering of the main cavity mode, which can be broadly grouped into two classes:

- (i) surface roughness, which are variations on the test mass surface responsible mostly for scattering at narrow angles, and
- (ii) point defects, which are “bright spots” on the mirror’s surface that produce diffuse scattering and are therefore responsible mostly for scattering at wide angles.

These imperfections on the test masses cause light to scatter out of the cavity and reflect multiple times off the beam tube wall as it propagates down the tube and eventually recombine with the main cavity mode at the opposite test mass. Seismic motion of the beam tube imposes a phase noise on the scattered light each time it reflects off the tube and gives rise to readout noise when the light recombines. Scattering of this nature was first pointed out by Thorne as an important noise source for the LIGO beam tubes (see Sec. III. B. of [110]). To address this, baffles were installed at various points along the LIGO beam tubes to deflect scattered light away from the test masses. However, the baffles give rise to *backscattering noise*, whereby light that is scattered out of the cavity by one of the test masses is backscattered off one of the baffles and subsequently recombines with the main cavity mode at the same test mass. Motion of the beam tube then imposes a phase noise on the backscattered light, which gives rise to readout noise when the light recombines. A detailed explanation of this effect is given by Flanagan and Thorne [111] and a detailed analysis of backscattering specifically for Cosmic Explorer is given in a recent technical report [112], which we summarize below. The effect of forward scattering, meaning the diffraction of the main beam whose time dependence arises primarily from seismically induced transverse motion of the baffles, is left for future work [113,114]. Additionally, the phase information of the baffle surfaces is not considered in this work, though simulations on Advanced LIGO indicate that the inclusion of this information can cause the scatter-induced strain noise power spectral density to fluctuate by an order of magnitude in either direction [115].

The fractional power scattered per unit solid angle is quantified by the bidirectional reflectance distribution function (BRDF), and the power spectrum of noise due to back scattered light is $S \propto \beta \kappa S_{\xi}$, where β is the BRDF of

the backscattering surface (i.e., the baffles and beam tube) and κ is related to the square of the mirror BRDF. Furthermore, S_{ξ} is the longitudinal displacement noise of the beam tube, taking into account fringe wrapping as explained in [116] and Sec. 3.1 of [112]. Here we use beam tube motion measured from the LIGO Livingston observatory, but the Cosmic Explorer baffles can be suspended to reduce their motion if necessary. Cosmic Explorer will likely use baffles with a black nickel coating with a BRDF of 10^{-3} sr^{-1} [117], however, diamondlike carbon coatings with a BRDF of 10^{-4} sr^{-1} can be used if necessary.

Surface roughness of spatial frequency ν gives rise to scattering at angle $\theta \sim \lambda \nu$, where λ is the optical wavelength, and θ is measured relative to the beam tube axis. The BRDF for this small angle scattering due to surface roughness is proportional to the PSD of the mirror surface variations at spatial frequency ν . The left panel of Fig. 16 shows the noise due to surface scattering using the surface PSD shown in Fig. 15, assuming a 120 cm tube diameter and 100 cm baffle aperture diameter. This PSD, with functional form $S(\nu) = (0.03 \text{ nm}^2 \text{ mm}) / (1 \text{ mm} \times \nu)$, is an upper limit requirement on the surface roughness over an appropriate range of spatial scales that scatter into the tube, based on Sec. 2.2 of [112], which results in noise due to surface scattering that is at least a factor of 10 below the design sensitivity at all frequencies. This requirement is comparable to the surface roughness that has already been achieved with the Advanced LIGO test masses at spatial scales below a few centimeters. (Comparison is harder at

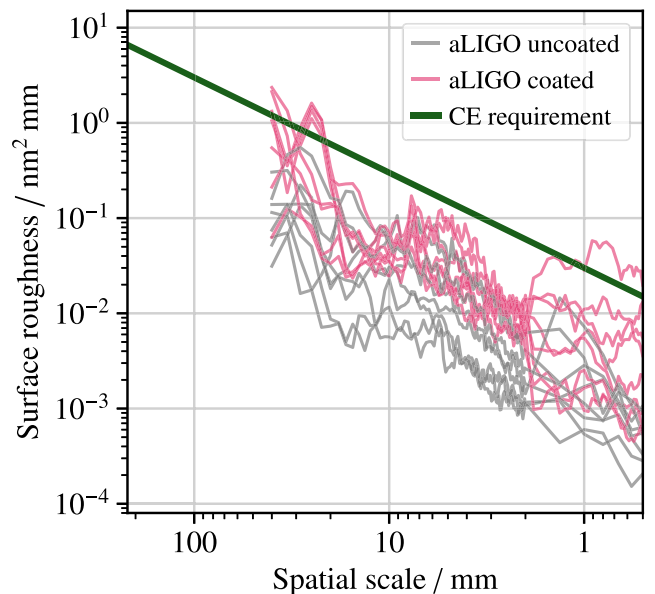


FIG. 15. Requirement on surface roughness used to calculate small angle scattering shown in Fig. 16, along with the measured spectra from Advanced LIGO test masses. Due to Cosmic Explorer’s large beam sizes, the relevant spatial scale (inverse spatial frequency) of the mirror roughness extends to several tens of centimeters.

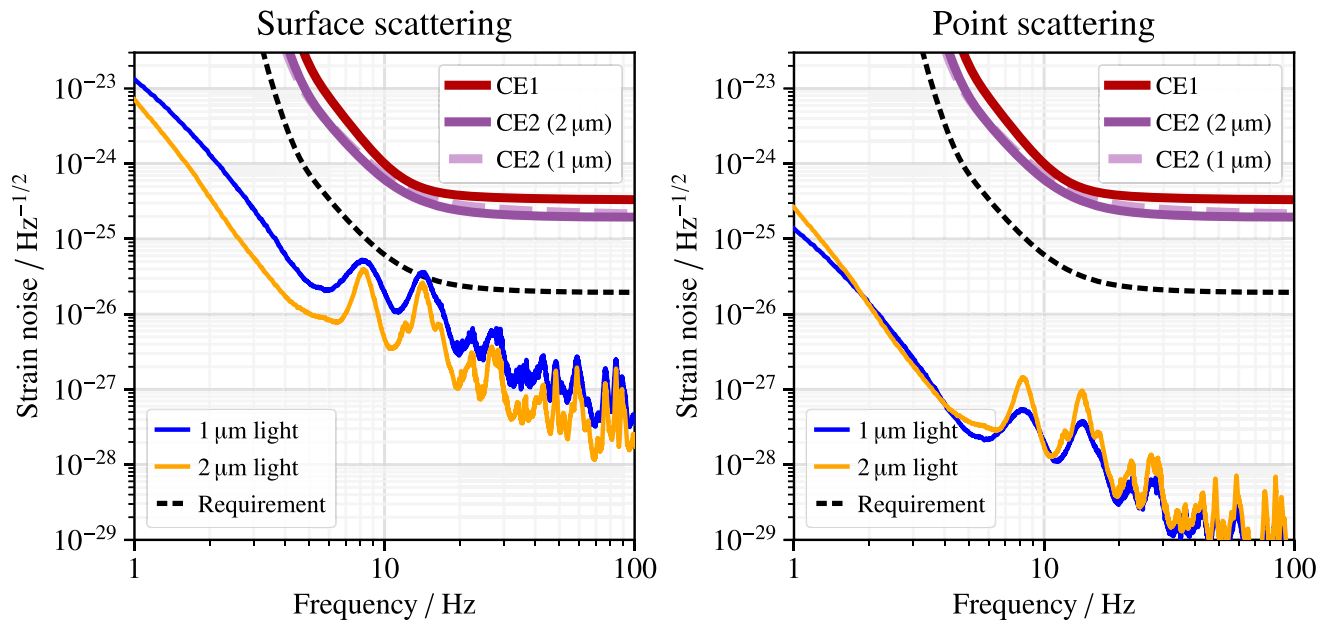


FIG. 16. Backscattering noise for surface roughness (left) and point defects (right) for a 120 cm diameter beam tube with 100 cm diameter baffle apertures. The black dashed curve shows the facility requirement that the scattering noise be a factor of 10 below the minimum of the three design noise curves shown for Cosmic Explorer. The BRDF for surface roughness scattering is proportional to the target PSD shown in Fig. 15 and the point scattering BRDF is 10^{-4} sr^{-1} . The BRDF of the baffles and beam tube is 10^{-3} sr^{-1} . The peaks are due to beam tube resonances.

larger spatial scales, where the Advanced LIGO surface roughness is not well characterized.)

Point defects give rise to diffuse scattering, which has a roughly constant BRDF. The right panel of Fig. 16 shows the scattered-light noise due to point defects assuming a mirror BRDF of 10^{-4} sr^{-1} and a 120 cm tube diameter. It appears that diffuse scattering is an insignificant noise source for all phases of Cosmic Explorer.

The choice of beam tube diameter is of particular importance for the design of Cosmic Explorer. While wider tubes lead to less scattering noise, they are also substantially more expensive considering the cost of the vacuum envelope, the metal needed for the tube, and the market availability of various tube dimensions. Figure 16 shows that a 120 cm diameter tube is sufficient to keep the backscattering noise below the noise requirements for both phases of the interferometer, provided that the requirements on mirror surface roughness are met. This limit on beam tube size will be reevaluated once the effects of forward scattering are considered.

H. Noise associated with controls

As a practical matter, the relative distances between the suspended optics as well as their angular alignment must be precisely servo controlled in order to keep the interferometer stable and operating in the linear regime. Noise from the sensors used to measure the linear and angular degrees of freedom is imposed on the optics by the control systems needed to suppress their relative positions and orientations.

In addition to the differential arm motion of the four test masses, there are three auxiliary length degrees of freedom of the other core optics, which are suspended from triple pendulum suspensions, that must be controlled. These degrees of freedom are limited by seismic noise below a few hertz and by sensing noise (of similar magnitude to that of Advanced LIGO) at higher frequencies. The auxiliary degree of freedom with the strongest coupling to the differential arm motion is the Michelson degree of freedom: differential motion between the beam splitter and the input test masses also produce phase fluctuations at the anti-symmetric port. The Michelson degree of freedom is suppressed by a factor of $\pi/2\mathcal{F} \simeq 3.5 \times 10^{-3}$ relative to the differential arm motion since the latter is enhanced by the Fabry-Perot arm cavities. The Michelson sensing noise is of order $10^{-16} \text{ m Hz}^{-1/2}$ [118], which gives an equivalent strain sensitivity of $\sim 6 \times 10^{-24} \text{ Hz}^{-1/2}$. Simulations show that if this motion is sensed and subtracted from the differential arm motion, a control loop with a bandwidth of a few hertz is sufficient to suppress the Michelson noise to within a factor of 10 below the design sensitivities for both CE1 and CE2. Simulations also suggest that the couplings of the other two auxiliary length degrees of freedom, fluctuations in the power-recycling and signal extraction cavity lengths, do not significantly couple to the differential arm motion through the fundamental optical mode.

The noise from the angular control systems is one of the most challenging low-frequency technical noise

sources in current gravitational-wave detectors, and it is also expected to be so for third-generation detectors. Radiation pressure from the circulating arm power exerts a torque on the mirrors. This torque stiffens (or hardens) the torsional resonance when the cavity mirrors rotate with the same sign and softens the resonance when the mirrors rotate with opposite sign [119–122]. The hard and soft resonances are shifted by $\Delta f_{h,s}^2 = \gamma_{h,s} P_{\text{arm}} L_{\text{arm}} / Ic$, where I is the moment of inertia of the mirrors, $\gamma_h > 0$ is a geometric factor for the hard mode, and $\gamma_s < 0$ is a geometric factor for the soft mode. The soft mode will become unstable if the torque is large enough and the (negative) shift Δf_s^2 exceeds the mechanical resonance f_0^2 . In this case, the bandwidth of the angular control loop needs to be several times the frequency of this unstable mode in order to stabilize the optomechanical system. Achieving this requirement without injecting excess sensing noise is challenging.

It is thus clearly advantageous to prevent the soft mode from becoming unstable. In this case the control loop bandwidth needs to be $\sim 3f_s$ [12]. One way to achieve this is to reduce the frequency shift Δf_s^2 . The arm power and length are set and the geometric factor is constrained by the necessity of minimizing the beam spot sizes. However, the moment of inertia can be increased, perhaps by increasing the test mass thickness or altering the geometry in some other way. Another possibility is to increase the free torsional resonance f_0 . The soft mode frequency shifts Δf_s^2 are approximately $-(0.6 \text{ Hz})^2$ for the $1 \mu\text{m}$ technology and $-(1.0 \text{ Hz})^2$ for the $2 \mu\text{m}$ technology. The soft mode will thus be stable, necessitating a sufficiently low loop bandwidth of a few hertz, if $f_0 \gtrsim 1 \text{ Hz}$.

Even though the frequency shift Δf_h^2 for the hard mode is always positive and the hard mode always stable, it can still be excited and must be damped. Two factors make this requirement intrinsically easier for Cosmic Explorer than for Advanced LIGO. First, the typical amplitude of these excitations will be less due to the improved seismic isolation. Second, the geometric factor for the hard mode is, to first order, proportional to $(w/w_0)^4$ where w_0 and w are the beam radii at the waist and at an optic, respectively [119]. The ratio w/w_0 needs to be small for CE to reduce diffraction over 40 km, while for Advanced LIGO it is made large to reduce coating thermal noise. This results in hard mode frequency shifts Δf_h^2 of approximately $+(1.1 \text{ Hz})^2$ for the $1 \mu\text{m}$ technology and $+(2.1 \text{ Hz})^2$ for the $2 \mu\text{m}$ technology.

We have only sketched the requirements for the control system and its noise performance here; while these preliminary considerations suggest that it will be possible to meet the low-frequency requirements, a realistic understanding of the control noise is a significant source of uncertainty facing Cosmic Explorer and warrants a more detailed analysis.

VI. DISCUSSION AND CONCLUSION

In this work we have presented updated sensitivity curves for Cosmic Explorer and have also identified several areas of research and development that will be necessary to realize its low-frequency performance:

- (i) the identification of a facility site with low seismic and acoustic noise, and other suitable environmental properties,
- (ii) the development of low-noise inertial isolators in multiple degrees of freedom,
- (iii) the continued development of mitigation techniques for Newtonian noise,
- (iv) the production of large, high-quality test mass substrates, both silica and silicon,
- (v) the polishing and coating of large test mass substrates to a resulting spatial roughness comparable to that achieved for the Advanced LIGO test masses, but characterized at larger spatial scales,
- (vi) the development of suitable mirror coatings,
- (vii) the development of long multistage suspensions employing highly stressed silica and silicon blade springs and silica fibers and silicon ribbons to support 320 kg test masses,
- (viii) the development of alternatives to blade spring suspensions, such as geometric antisprings,
- (ix) the validation and extension of the beam tube scattering model presented here,
- (x) the development of a robust angular control system with possible modifications to the suspensions and/or test masses to reduce the effects of radiation-pressure instabilities,
- (xi) the development of vacuum technology and practice capable of achieving ultrahigh vacuum in both the test mass chambers, which will be periodically vented, and the beam tubes,
- (xii) the measurement of material properties, such as mechanical loss angles, down to 5 Hz, and
- (xiii) the development of laser frequency and intensity noise requirements and the optical topologies required to achieve them not discussed here.

Table III summarizes the research required to reach the low-frequency sensitivity presented here along with a rough time line of when that research would need to be completed.

We have also shown that both the 1 and $2 \mu\text{m}$ technologies can realize nearly identical low-frequency sensitivities for CE2. While this is true for high frequencies as well, achieving the specified quantum and thermal noise performance for both technologies requires further research and development not discussed in this paper. Additionally, if the arm length of Cosmic Explorer were significantly shortened, the relative importance of the various noise sources may change since they scale differently with arm length [17].

TABLE III. Summary of required research and development activities. The final columns in the table indicate whether the activity involves primarily the facility, the initial Cosmic Explorer detector (CE1), or the advanced Cosmic Explorer detector (CE2); for the advanced detector, activities are presented for both the scenario in which the detector is room-temperature glass technology with 1 μm lasers or cryogenic silicon technology with 2 μm lasers.

Activity	Theme	Facility	CE1	CE2(1)	CE2(2)
Partial pressures of gases (IV C)	Vacuum	•			
Ambient seismic field characterization, including surface and body-wave content (IVA)	Seismic arrays	•			
Ambient infrasound field characterization, distinguished from wind-induced sensor noise (IV B)	Infrasound arrays	•			
Reduction of seismic field near test masses (V C 3)	Seismic metamaterials	•			
Reduction of magnetic field coupling	Other environmental	•			
1 pm Hz ^{-1/2} horizontal suspension point motion at 1 Hz (V B)	Inertial sensing		•		
2× subtraction of surface-wave Newtonian noise (V C 1)	Seismic arrays		•		
1.5 MW 1 μm arm power and 6 dB frequency-dependent squeezing (silica)	Quantum noise, scatter		•		
Silica test mass, 70 cm \varnothing ; low impurity	Silica materials science		•	•	
Highly stressed silica blade springs (VA)	Silica materials science		•	•	
Validation of silica loss mechanisms at 5 Hz	Silica materials science		•	•	
A+ coatings over 70 cm \varnothing (V D 2)	Thin-film mirror coatings		•	•	
Test mass surface polishing of large substrates (V G)	Mirror metrology		•	•	•
Control noise	Optical sensing and control		•	•	•
10× subtraction of surface-wave Newtonian noise (V C 1)	Seismic arrays			•	•
3× subtraction of body-wave Newtonian noise (V C 1)	Seismic arrays			•	•
Best effort at mitigation of infrasound Newtonian noise	Infrasound arrays	•		•	•
0.1 pm Hz ^{-1/2} horizontal suspension point motion at 1 Hz (V B)	Inertial sensing			•	•
1.5 MW 1 μm arm power and 10 dB frequency-dependent squeezing (silica)	Quantum noise, scatter			•	
Silicon test mass, 80 cm \varnothing ; low impurity	Silicon materials science				•
Highly stressed silicon blade springs and ribbons (VA)	Silicon materials science				•
Validation of silicon loss mechanisms at 5 Hz	Silicon materials science				•
“Voyager” coatings over 80 cm \varnothing (V D 2)	Thin-film mirror coatings				•
3.0 MW 2 μm arm power and 10 dB frequency-dependent squeezing (silicon)	Quantum noise, scatter				•
Radiative temperature control to ± 2 K (V D 1)	Cryogenics	•			•

ACKNOWLEDGMENTS

The authors gratefully acknowledge the support of the National Science Foundation through collaborative Grants No. 1836814, No. 1836809, No. 1836734, and No. 1836702. E. D. H. is supported by the MathWorks, Inc. J. R. S. is partially supported by the Dan Black Family Trust. Y. B. is supported by the Sherman Fairchild Fellowship and by the U.S. Department of Energy, Office of Science, Office of High Energy Physics, under Award No. DE-SC0011632. B. K. is supported by the Heising-Simons Foundation. B. J. J. S. is supported through Australian Research Council (ARC) Centre of Excellence CE170100004.

APPENDIX A: SUMMARY OF COSMIC EXPLORER TECHNOLOGIES

One advantage of realizing Cosmic Explorer incrementally is that CE1 can achieve significantly higher sensitivities than the second-generation detectors mostly using the

existing technology developed for LIGO A+. In addition to providing a relatively short route to increased sensitivity, this provides some risk management: significant improvements can still be made even if some advanced technologies are not realized. Nevertheless, the baseline CE1 design does rely on some technological advances beyond A+. We can also consider a more conservative detector, CE1-, which relies solely on A+ technology with the improved sensitivity coming only from scaling up the arm length, test masses, and suspensions from the A+ design. In particular, this would differ from CE1 by the following:

- (i) no fused silica blade springs on the final suspension stage between the PUM and the test mass; the suspensions are just a scaled up version of the A+ suspensions,
- (ii) no Newtonian Rayleigh-wave suppression,
- (iii) the same level of suspension point motion as A+, a factor of 10 worse than CE1 at 1 Hz.

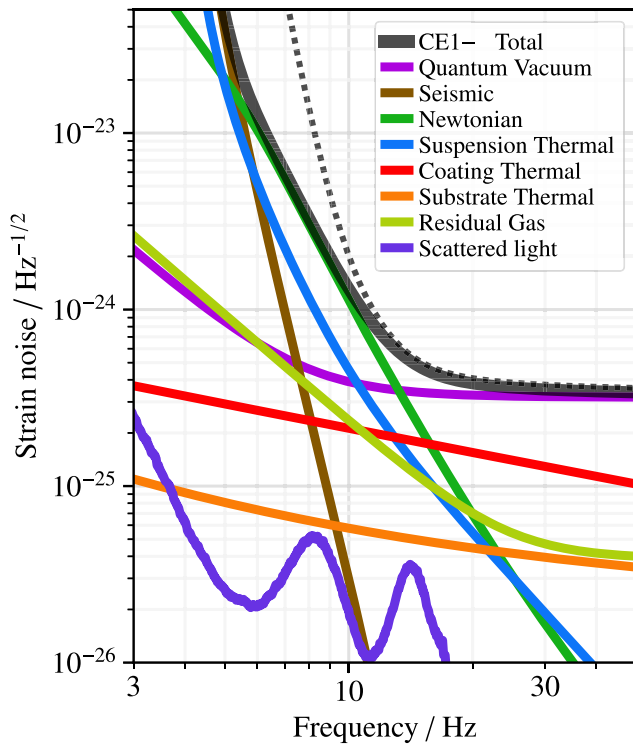


FIG. 17. Estimated low-frequency spectral sensitivity limit (solid black) of Cosmic Explorer 1—and the known noise sources that cause these limits (colored curves). The sensitivity limit for Cosmic Explorer 1 from previous work [17] is also shown (dotted black curve).

Figure 17 shows the low-frequency limit to the spectral sensitivity of CE1—. These changes only affect the low-frequency noise below about 20 Hz leaving identical high-frequency sensitivities for CE1 and CE1—. This can

also be thought of as an initial detector to be implemented first while some of the above technologies are being developed for CE1 if necessary.

A summary of the defining parameters of the different Cosmic Explorer detectors and technologies is given in Table IV and their sensitivities compared in Fig. 18; many of the other details common to all detectors using the same technology are given in Table II. All of the $1\ \mu\text{m}$ detectors share the same basic properties: arm power, material, temperature, coatings, and beam spot sizes. The low-frequency sensitivity of CE1 is improved over CE1— by the addition of fused silica blades springs, which reduce the suspension thermal and seismic noises as described in Secs. VA and VB, improved seismic isolation, as discussed in Sec. VB, and some suppression of Newtonian Rayleigh waves, as discussed in Sec. VC. The test mass thermal noises, most importantly coating Brownian, are the same for all detectors using $1\ \mu\text{m}$ technology since they use the same test mass substrates and coatings, beam sizes, and temperatures.

The high-frequency sensitivity of CE2 is nearly identical for both the 1 and $2\ \mu\text{m}$ technologies since this is determined by quantum shot noise. The $1\ \mu\text{m}$ realization of CE2 has the same squeezing as the $2\ \mu\text{m}$ realization: $10\ \text{dB}$ increased from $6\ \text{dB}$ for CE1. Since the shot noise scales as $S \propto \lambda/P_{\text{arm}}$, the factor of 2 larger power stored in the arms of the $2\ \mu\text{m}$ realization gives the same shot noise level as the $1\ \mu\text{m}$ realization. All other technologies not dependent on test mass material or laser wavelength are the same for both realizations of CE2. In particular, the seismic isolation is improved over that of CE1 by a factor of 10 at $1\ \text{Hz}$, Newtonian body waves are suppressed by a factor of 3, and Newtonian Rayleigh waves are suppressed by an additional factor of 5 over that of CE1. Both realizations thus have the same Newtonian noise.

TABLE IV. Defining parameters of the different Cosmic Explorer technologies and detectors. See Table II for more details common to all detectors using the same technology.

Quantity	Units	CE1-	CE1	CE2 ($1\ \mu\text{m}$)	CE2 ($2\ \mu\text{m}$)
Arm power	MW	1.5	1.5	1.5	3
Wavelength	μm	1	1	1	2
Squeezing	dB	6	6	10	10
Material		Silica	Silica	Silica	Silicon
Temperature	K	293	293	293	123
Final stage blade		No	Yes	Yes	Yes
Rayleigh-wave suppression		None	$2\times$	$10\times$	$10\times$
Body-wave suppression		None	None	$3\times$	$3\times$
Suspension point at $1\ \text{Hz}$	$\text{pm Hz}^{-1/2}$	10	1	0.1	0.1
Coatings		A+	A+	A+	Voyager
ITM spot size	cm	12	12	12	16
ETM spot size	cm	12	12	12	16

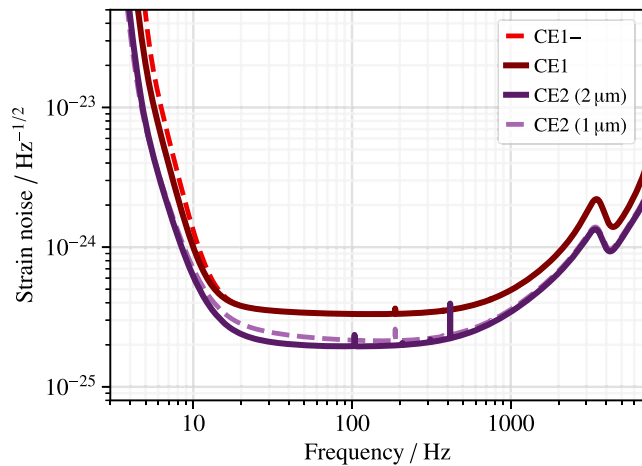


FIG. 18. Strain sensitivities of the different Cosmic Explorer technologies and detectors.

To summarize, the low-frequency sensitivity is dominated by suspension thermal, seismic, and Newtonian noise. The low-frequency sensitivity of CE1 is improved over that of CE1- due to improved suspensions, seismic isolation, and the addition of Newtonian noise suppression. The low-frequency sensitivity of CE2 is improved over that of CE1 through further improvements to the seismic isolation and Newtonian noise suppression and increased squeezing. Since the high-frequency sensitivity is determined by quantum shot noise, CE1 and CE1- have the same high-frequency sensitivity, as do both realizations of CE2.

APPENDIX B: DISPLACEMENT AND FORCE SENSITIVITY

Figure 19 compares the noise of Cosmic Explorer, Advanced LIGO, and Voyager in terms of gravitational-wave strain and the equivalent test mass displacement and force noises. To achieve its design sensitivity above ~ 20 Hz, Cosmic Explorer does not require as low displacement or force noise as does Voyager, owing to the longer arms and larger test masses. However, significant improvements in displacement and force noises are required to achieve the Cosmic Explorer strain sensitivity at lower frequencies.

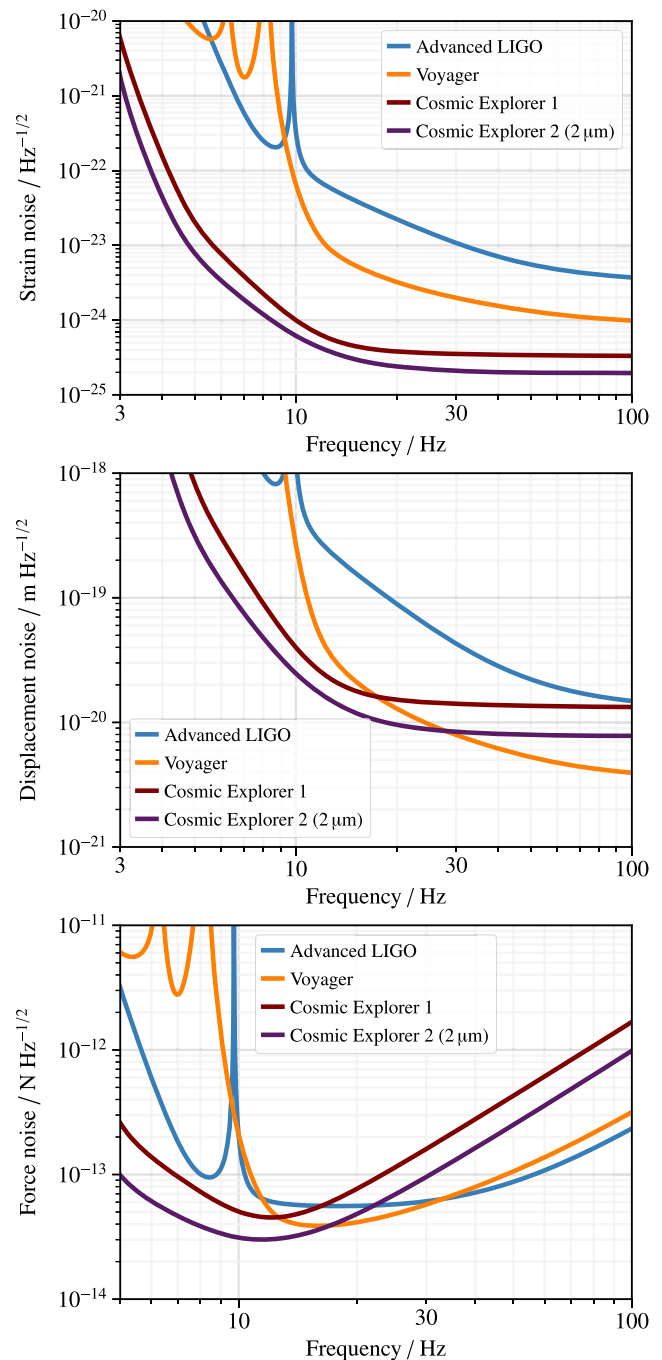


FIG. 19. Comparison of Cosmic Explorer strain, displacement, and force noises with those of Advanced LIGO and Voyager.

[1] J. Aasi, B. P. Abbott, R. Abbott, T. Abbott, M. R. Abernathy, K. Ackley, C. Adams, T. Adams, P. Addesso *et al.* (LIGO Scientific Collaboration), *Classical Quantum Gravity* **32**, 074001 (2015).

[2] F. Acernese, M. Agathos, K. Agatsuma, D. Aisa, N. Allemandou, A. Allocca, J. Amarni, P. Astone, G. Balestri, G. Ballardin *et al.*, *Classical Quantum Gravity* **32**, 024001 (2015).

- [3] T. Akutsu *et al.* (Kagra Collaboration), *Nat. Astron.* **3**, 35 (2019).
- [4] B. P. Abbott, R. Abbott, T. D. Abbott, M. R. Abernathy, F. Acernese, K. Ackley, C. Adams, T. Adams, P. Addesso, R. X. Adhikari *et al.*, *Phys. Rev. Lett.* **116**, 061102 (2016).
- [5] B. P. Abbott, R. Abbott, T. D. Abbott, M. R. Abernathy, F. Acernese, K. Ackley, C. Adams, T. Adams, P. Addesso, R. X. Adhikari *et al.*, *Phys. Rev. X* **6**, 041015 (2016).
- [6] B. P. Abbott, R. Abbott, T. D. Abbott, F. Acernese, K. Ackley, C. Adams, T. Adams, P. Addesso, R. X. Adhikari, V. B. Adya *et al.*, *Phys. Rev. Lett.* **119**, 161101 (2017).
- [7] B. P. Abbott, R. Abbott, T. D. Abbott, F. Acernese, K. Ackley, C. Adams, T. Adams, P. Addesso, R. X. Adhikari, V. B. Adya *et al.*, *Astrophys. J. Lett.* **848**, L12 (2017).
- [8] B. P. Abbott, R. Abbott, T. D. Abbott, S. Abraham, F. Acernese, K. Ackley, C. Adams, R. X. Adhikari, V. B. Adya, C. Affeldt *et al.*, *Phys. Rev. X* **9**, 031040 (2019).
- [9] A. H. Nitz, C. Capano, A. B. Nielsen, S. Reyes, R. White, D. A. Brown, and B. Krishnan, *Astrophys. J.* **872**, 195 (2019).
- [10] B. P. Abbott, R. Abbott, T. D. Abbott, S. Abraham, F. Acernese, K. Ackley, C. Adams, R. X. Adhikari, V. B. Adya, C. Affeldt *et al.*, *Astrophys. J.* **875**, 161 (2019).
- [11] J. Miller, L. Barsotti, S. Vitale, P. Fritschel, M. Evans, and D. Sigg, *Phys. Rev. D* **91**, 062005 (2015).
- [12] R. X. Adhikari *et al.*, *Classical Quantum Gravity* **37**, 165003 (2020).
- [13] K. Ackley *et al.*, *Pub. Astron. Soc. Aust.* **37**, e047 (2020).
- [14] The GWIC 3G Science Case Team Consortium, The next-generation global gravitational-wave observatory: New astrophysics with the farthest, oldest, and most violent events in the universe, Technical Report, GWIC, 2019.
- [15] GWIC, GWIC-3G, GWIC-3G-R&D-Consortium, 3G R&D: Research and development for the next generation of ground-based gravitational-wave detectors, Technical Report, GWIC, 2019.
- [16] S. Hild *et al.*, *Classical Quantum Gravity* **28**, 094013 (2011).
- [17] B. P. Abbott, R. Abbott, T. D. Abbott, M. R. Abernathy, K. Ackley, C. Adams, P. Addesso, R. X. Adhikari, V. B. Adya, C. Affeldt *et al.*, *Classical Quantum Gravity* **34**, 044001 (2017).
- [18] D. Reitze *et al.*, *Bull. Am. Astron. Soc.* **51**, 141 (2019), <https://baas.aas.org/pub/2020n3i141>.
- [19] D. Reitze *et al.*, *Bull. Am. Astron. Soc.* **51**, 35 (2019), <https://baas.aas.org/pub/2020n7i035>.
- [20] L. A. Wainstein and V. D. Zubakov, *Extraction of Signals from Noise* (Dover, New York, NY, 1970).
- [21] L. S. Finn and D. F. Chernoff, *Phys. Rev. D* **47**, 2198 (1993).
- [22] J. Creighton and W. Anderson, *Gravitational-Wave Physics and Astronomy: An Introduction to Theory, Experiment and Data Analysis* (Wiley-VCH, Weinheim, 2011).
- [23] C. Cutler and É. E. Flanagan, *Phys. Rev. D* **49**, 2658 (1994).
- [24] R. Abbott, T. D. Abbott, S. Abraham, F. Acernese, K. Ackley, A. Adams, C. Adams, R. X. Adhikari *et al.* (The LIGO Scientific and Virgo Collaborations), [arXiv:2010.14533](https://arxiv.org/abs/2010.14533).
- [25] A. Sesana, J. Gair, I. Mandel, and A. Vecchio, *Astrophys. J. Lett.* **698**, L129 (2009).
- [26] H.-Y. Chen, D. E. Holz, J. Miller, M. Evans, S. Vitale, and J. Creighton, *Classical Quantum Gravity* **38**, 055010 (2021).
- [27] D. Marković, *Phys. Rev. D* **48**, 4738 (1993).
- [28] K. Izumi and D. Sigg, *Classical Quantum Gravity* **34**, 015001 (2017).
- [29] F. Amann *et al.*, *Rev. Sci. Instrum.* **91**, 094504 (2020).
- [30] J. Harms, *Living Rev. Relativity* **22**, 6 (2019).
- [31] A. Meltzer, R. Rudnick, P. Zeitler, A. Levander, G. Humphreys, K. Karlstrom, E. Ekstrom, C. Carlson, T. Dixon, M. Gurnis *et al.*, *Geol. Soc. Am. Today* **9**, 8 (1999).
- [32] H. Benz, R. Buland, J. Filson, A. Frankel, and K. Shedlock, *Seismol. Res. Lett.* **72**, 70 (2001).
- [33] P. Nguyen, R. M. S. Schofield, A. Effler, C. Austin, V. Adya, M. Ball, S. Banagiri, K. Banowetz, C. Billman, C. D. Blair *et al.*, [arXiv:2101.09935](https://arxiv.org/abs/2101.09935).
- [34] J. R. Peterson, Observations and modeling of seismic background noise, U.S. Geological Survey Open-File Report 93-322, 1993, <https://doi.org/10.3133/ofr93322>.
- [35] S. Bonnefoy-Claudet, F. Cotton, and P.-Y. Bard, *Earth-Sci. Rev.* **79**, 205 (2006).
- [36] J. R. Bowman, G. E. Baker, and M. Bahavar, *Geophys. Res. Lett.* **32**, L09803 (2005).
- [37] T. Creighton, *Classical Quantum Gravity* **25**, 125011 (2008).
- [38] M. E. Zucker and S. E. Whitcomb, in *Proceedings of the Seventh Marcel Grossman Meeting on Recent Developments in Theoretical and Experimental General Relativity, Gravitation, and Relativistic Field Theories*, edited by R. T. Jantzen, G. Mac Keiser, and R. Ruffini (World Scientific, Singapore, 1996), p. 1434.
- [39] R. Takahashi, Y. Saito, M. Fukushima, M. Ando, K. Arai, D. Tatsumi, G. Heinzel, S. Kawamura, T. Yamazaki, and S. Moriwaki, *J. Vac. Sci. Technol.* **20**, 1237 (2002).
- [40] A. Cavalleri, G. Ciani, R. Dolesi, M. Hueller, D. Nicolodi, D. Tombolato, S. Vitale, P. J. Wass, and W. J. Weber, *Phys. Lett. A* **374**, 3365 (2010).
- [41] R. Dolesi, M. Hueller, D. Nicolodi, D. Tombolato, S. Vitale, P. J. Wass, W. J. Weber, M. Evans, P. Fritschel, R. Weiss, J. H. Gundlach, C. A. Hagedorn, S. Schlamminger, G. Ciani, and A. Cavalleri, *Phys. Rev. D* **84**, 063007 (2011).
- [42] S. M. Aston *et al.*, *Classical Quantum Gravity* **29**, 235004 (2012).
- [43] H. B. Callen and T. A. Welton, *Phys. Rev.* **83**, 34 (1951).
- [44] H. B. Callen and R. F. Greene, *Phys. Rev.* **86**, 702 (1952).
- [45] G. I. González and P. R. Saulson, *Acoust. Soc. Am. J.* **96**, 207 (1994).
- [46] G. González, *Classical Quantum Gravity* **17**, 4409 (2000).
- [47] J. M. Gere and S. P. Timoshenko, *Mechanics of Materials*, 4th ed. (PWS Publishing Company, Boston, 1997).
- [48] P. R. Saulson, *Phys. Rev. D* **42**, 2437 (1990).
- [49] A. M. Gretarsson, G. M. Harry, S. D. Penn, P. R. Saulson, W. J. Startin, S. Rowan, G. Cagnoli, and J. Hough, *Phys. Lett. A* **270**, 108 (2000).
- [50] K. V. Tokmakov, A. Cumming, J. Hough, R. Jones, R. Kumar, S. Reid, S. Rowan, N. A. Lockerbie, A. Wanner, and G. Hammond, *J. Non-Cryst. Solids* **358**, 1699 (2012).

- [51] K.-H. Lee, G. Hammond, J. Hough, R. Jones, S. Rowan, and A. Cumming, *Classical Quantum Gravity* **36**, 185018 (2019).
- [52] A. V. Cumming, L. Cunningham, G. D. Hammond, K. Haughian, J. Hough, S. Kroker, I. W. Martin, R. Nawrodt, S. Rowan, C. Schwarz, and A. A. van Veggel, *Classical Quantum Gravity* **31**, 025017 (2014).
- [53] J. C. McLaughlin and A. F. W. Willoughby, *J. Cryst. Growth* **85**, 83 (1987).
- [54] F. W. DelRio, R. F. Cook, and B. L. Boyce, *Appl. Phys. Rev.* **2**, 021303 (2015).
- [55] G. Cella, R. DeSalvo, V. Sannibale, H. Tariq, N. Viboud, and A. Takamori, *Nucl. Instrum. Methods Phys. Res., Sect. A* **487**, 652 (2002).
- [56] F. Matichard *et al.*, *Classical Quantum Gravity* **32**, 185003 (2015).
- [57] C. M. Mow-Lowry and D. Martynov, *Classical Quantum Gravity* **36**, 245006 (2019).
- [58] S. J. Cooper, C. J. Collins, A. C. Green, D. Hoyland, C. C. Speake, A. Freise, and C. M. Mow-Lowry, *Classical Quantum Gravity* **35**, 095007 (2018).
- [59] K. Venkateswara, C. A. Hagedorn, M. D. Turner, T. Arp, and J. H. Gundlach, *Rev. Sci. Instrum.* **85**, 015005 (2014).
- [60] M. W. Coughlin, J. Harms, J. Driggers, D. J. McManus, N. Mukund, M. P. Ross, B. J. J. Slagmolen, and K. Venkateswara, *Phys. Rev. Lett.* **121**, 221104 (2018).
- [61] M. P. Ross, K. Venkateswara, C. Mow-Lowry, S. Cooper, J. Warner, B. Lantz, J. Kissel, H. Radkins, T. Shaffer, R. Mittleman, A. Pele, and J. Gundlach, *Classical Quantum Gravity* **37**, 185018 (2020).
- [62] J. V. van Heijningen, A. Bertolini, and J. F. J. van den Brand, in *2018 IEEE Sensors Applications Symposium (SAS)* (Curran, Red Hook, 2018), pp. 1–5.
- [63] J. V. van Heijningen, *J. Instrum.* **15**, P06034 (2020).
- [64] H. Yu, D. Martynov, S. Vitale, M. Evans, D. Shoemaker, B. Barr, G. Hammond, S. Hild, J. Hough, S. Huttner, S. Rowan, B. Sorazu, L. Carbone, A. Freise, C. Mow-Lowry, K. L. Dooley, P. Fulda, H. Grote, and D. Sigg, *Phys. Rev. Lett.* **120**, 141102 (2018).
- [65] J. C. Driggers, J. Harms, and R. X. Adhikari, *Phys. Rev. D* **86**, 102001 (2012).
- [66] J. Harms and S. Hild, *Classical Quantum Gravity* **31**, 185011 (2014).
- [67] S. Brûlé, E. H. Javelaud, S. Enoch, and S. Guenneau, *Phys. Rev. Lett.* **112**, 133901 (2014).
- [68] A. Colombi, D. Colquitt, P. Roux, S. Guenneau, and R. V. Craster, *Sci. Rep.* **6**, 27717 (2016).
- [69] A. Palermo, S. Krödel, A. Marzani, and C. Daraio, *Sci. Rep.* **6**, 39356 (2016).
- [70] P. Roux, D. Bindi, T. Boxberger, A. Colombi, F. Cotton, I. Douste-Bacque, S. Garambois, P. Gueguen, G. Hillers, D. Hollis *et al.*, *Seismol. Res. Lett.* **89**, 582 (2018).
- [71] B. Kamai, *Bull. Am. Phys. Soc.* **64**, R11.006 (2019).
- [72] R. Zacherini, A. Colombi, A. Palermo, V. K. Dertimanis, A. Marzani, H. R. Thomsen, B. Stojadinovic, and E. N. Chatzi, *Phys. Rev. Applied* **13**, 034055 (2020).
- [73] D. Fiorucci, in *GWADW 2019* (Elba, 2019).
- [74] D. Fiorucci, J. Harms, M. Barsuglia, I. Fiori, and F. Paoletti, *Phys. Rev. D* **97**, 062003 (2018).
- [75] G. R. Fowles, *Introduction to Modern Optics* (Dover, New York, 1968).
- [76] G. Harry, T. P. Bodiya, and R. DeSalvo, *Optical Coatings and Thermal Noise in Precision Measurement* (Cambridge University Press, Cambridge, 2012).
- [77] M. Granata, A. Amato, G. Cagnoli, M. Coulon, J. Degallaix, D. Forest, L. Mereni, C. Michel, L. Pinard, B. Sassolas, and J. Teillon, *Appl. Opt.* **59**, A229 (2020).
- [78] G. Vajente, M. Fazio, L. Yang, A. Ananyeva, G. Billingsley, A. Markosyan, R. Bassiri, M. Fejer, and C. Menoni, *Bull. Am. Phys. Soc.* **65**, W52.00002 (2020).
- [79] W. Yam, S. Gras, and M. Evans, *Phys. Rev. D* **91**, 042002 (2015).
- [80] S. C. Tait, J. Steinlechner, M. M. Kinley-Hanlon, P. G. Murray, J. Hough, G. McGhee, F. Pein, S. Rowan, R. Schnabel, C. Smith, L. Terkowski, and I. W. Martin, *Phys. Rev. Lett.* **125**, 011102 (2020).
- [81] S. Gras and M. Evans, *Phys. Rev. D* **98**, 122001 (2018).
- [82] V. B. Braginsky, M. L. Gorodetsky, and S. P. Vyatchanin, *Phys. Lett. A* **264**, 1 (1999).
- [83] A. Markowitz, Cryogenic cooling for LIGO voyager, Technical Report No. LIGO-G1801047-v3, LIGO Laboratory, Caltech, 2018.
- [84] D. S. Kim, O. Hellman, J. Herriman, H. L. Smith, J. Y. Y. Lin, N. Shulumba, J. L. Niedziela, C. W. Li, D. L. Abernathy, and B. Fultz, *Proc. Natl. Acad. Sci. U.S.A.* **115**, 1992 (2018).
- [85] T. Middelmann, A. Walkov, G. Bartl, and R. Schödel, *Phys. Rev. B* **92**, 174113 (2015).
- [86] M. Cheung, A. Markowitz, B. Kamai, and R. X. Adhikari, Real-time temperature monitoring of mechanical oscillators, Technical Report No. LIGO-T1800312-v2, LIGO Laboratory, 2018, SURF18 project.
- [87] V. B. Braginsky, M. L. Gorodetsky, and S. P. Vyatchanin, *Phys. Lett. A* **271**, 303 (2000).
- [88] D. Heinert, A. G. Gurkovsky, R. Nawrodt, S. P. Vyatchanin, and K. Yamamoto, *Phys. Rev. D* **84**, 062001 (2011).
- [89] V. B. Braginsky and S. P. Vyatchanin, *Phys. Lett. A* **324**, 345 (2004).
- [90] D. Heinert, A. Bell, G. Cagnoli, J. Degallaix, G. Gemme, S. Hild, J. Hough, H. Lück, I. W. Martin, S. Rowan, S. P. Vyatchanin, and R. Nawrodt, Free carrier driven noise in transmissive semiconductor optics, Technical Report No. LIGO-P1400084-v1, LIGO, 2014.
- [91] F. Bruns, S. P. Vyatchanin, J. Dickmann, R. Glaser, D. Heinert, R. Nawrodt, and S. Kroker, Thermal charge carrier driven noise in transmissive semiconductor optics, Technical Report No. LIGO-P2000048-v1, LIGO, 2020.
- [92] W. Winkler, A. Rüdiger, R. Schilling, K. A. Strain, and K. Danzmann, *Opt. Commun.* **112**, 245 (1994).
- [93] C. Krüger, D. Heinert, A. Khalaidovski, J. Steinlechner, R. Nawrodt, R. Schnabel, and H. Lück, *Classical Quantum Gravity* **33**, 015012 (2016).
- [94] T. Hong, H. Yang, E. K. Gustafson, R. X. Adhikari, and Y. Chen, *Phys. Rev. D* **87**, 082001 (2013).
- [95] M. Evans, S. Ballmer, M. Fejer, P. Fritschel, G. Harry, and G. Ogil, *Phys. Rev. D* **78**, 102003 (2008).
- [96] C. M. Caves, *Phys. Rev. D* **23**, 1693 (1981).
- [97] H. J. Kimble, Y. Levin, A. B. Matsko, K. S. Thorne, and S. P. Vyatchanin, *Phys. Rev. D* **65**, 022002 (2001).

- [98] A. Buonanno and Y. Chen, *Phys. Rev. D* **65**, 042001 (2002).
- [99] S. L. Danilishin and F. Y. Khalili, *Living Rev. Relativity* **15**, 5 (2012).
- [100] S. Hild, A basic introduction to quantum noise and quantum-non-demolition techniques, in *Advanced Interferometers and the Search for Gravitational Waves*, Vol. 404, edited by M. Bassan (Springer, Cham, 2014), p. 291.
- [101] H. Miao and Y. Chen, Quantum theory of laser interferometer gravitational wave detectors, in *Advanced Gravitational Wave Detectors*, edited by D. G. Blair, E. J. Howell, L. Ju, and C. Zhao (Cambridge University Press, Cambridge, England, 2012), p. 277–297.
- [102] R. Schnabel, *Phys. Rep.* **684**, 1 (2017).
- [103] L. Barsotti, J. Harms, and R. Schnabel, *Rep. Prog. Phys.* **82**, 016905 (2019).
- [104] M. Tse, H. Yu, N. Kijbunchoo, A. Fernandez-Galiana, P. Dupej, L. Barsotti, C. D. Blair, D. D. Brown, S. E. Dwyer, A. Effler *et al.*, *Phys. Rev. Lett.* **123**, 231107 (2019).
- [105] F. Acernese, M. Agathos, L. Aiello, A. Allocca, A. Amato, S. Ansoldi, S. Antier, M. Arène, N. Arnaud, S. Ascenzi *et al.*, *Phys. Rev. Lett.* **123**, 231108 (2019).
- [106] M. Evans, L. Barsotti, P. Kwee, J. Harms, and H. Miao, *Phys. Rev. D* **88**, 022002 (2013).
- [107] P. Kwee, J. Miller, T. Isogai, L. Barsotti, and M. Evans, *Phys. Rev. D* **90**, 062006 (2014).
- [108] E. Oelker, T. Isogai, J. Miller, M. Tse, L. Barsotti, N. Mavalvala, and M. Evans, *Phys. Rev. Lett.* **116**, 041102 (2016).
- [109] L. McCuller, C. Whittle, D. Ganapathy, K. Komori, M. Tse, A. Fernandez-Galiana, L. Barsotti, P. Fritschel, M. MacInnis, F. Matichard, K. Mason, N. Mavalvala, R. Mittleman, H. Yu, M. E. Zucker, and M. Evans, *Phys. Rev. Lett.* **124**, 171102 (2020).
- [110] K. Thorne, Light scattering and proposed baffle configuration for the LIGO, Technical Report No. LIGO-T890017-00-R, LIGO, 1981.
- [111] E. Flanagan and K. Thorne, Noise due to backscatter off baffles, the nearby wall, and objects at the far end of the beam tube, and recommended actions, Technical Report No. LIGO-T940063-00-R, LIGO, 1994.
- [112] Y. Bai, Cosmic explorer: Back-scatter noise and design recommendations, Technical Report No. LIGO-T1900854-v1, LIGO, 2019.
- [113] Éanna É. Flanagan and K. Thorne, Light scattering and baffle configuration for LIGO, Technical Report No. T950101, LIGO, 1995.
- [114] V. Nourrit, J. L. de Bougrenet de La Tocnaye, and P. Chanclou, *J. Opt. Soc. Am. A* **18**, 546 (2001).
- [115] R. Day, FFT simulation using FOG, Technical Report No. G1300532, LIGO, 2013.
- [116] D. J. Ottaway, P. Fritschel, and S. J. Waldman, *Opt. Express* **20**, 8329 (2012).
- [117] A. Ananyeva, BRDF vs R^2 of black Ni and DLC coatings samples on super#8 SSSL, Technical Report No. LIGO-T1700450, LIGO, 2019.
- [118] D. V. Martynov, E. D. Hall, B. P. Abbott, R. Abbott, T. D. Abbott, C. Adams, R. X. Adhikari, R. A. Anderson, S. B. Anderson, K. Arai *et al.*, *Phys. Rev. D* **93**, 112004 (2016).
- [119] J. A. Sidles and D. Sigg, *Phys. Lett. A* **354**, 167 (2006).
- [120] L. Barsotti, M. Evans, and P. Fritschel, *Classical Quantum Gravity* **27**, 084026 (2010).
- [121] E. Hirose, K. Kawabe, D. Sigg, R. Adhikari, and P. R. Saulson, *Appl. Opt.* **49**, 3474 (2010).
- [122] K. L. Dooley, L. Barsotti, R. X. Adhikari, M. Evans, T. T. Fricke, P. Fritschel, V. Frolov, K. Kawabe, and N. Smith-Lefebvre, *J. Opt. Soc. Am. A* **30**, 2618 (2013).